CANCER IMMUNOLOGY

Cancer immunotherapy via synergistic coactivation of myeloid receptors CD40 and Dectin-1

Max M. Wattenberg[1,2]*, Heather Coho[1,2], Veronica M. Herrera[1,2]†, Kathleen Graham[1,2], Meredith L. Stone[1,2], Yuqing Xue[1,2], Renee B. Chang[1,2], Christopher Cassella[1,2], Mingen Liu[1,2], Shaanti Choi-Bose[1,2], Stacy K. Thomas[1,2], Hana Choi[1,2], Yan Li[1,2], Kelly Markowitz[1,2], Lauren Melendez[1,2], Michael Gianonne[1,2], Nandita Bose[3], Gregory L. Beatty[1,2]*

Myeloid cells facilitate T cell immune evasion in cancer yet are pliable and have antitumor potential. Here, by cotargeting myeloid activation molecules, we leveraged the myeloid compartment as a therapeutic vulnerability in mouse models of pancreatic cancer. Myeloid cells in solid tumors expressed activation receptors including the pattern recognition receptor Dectin-1 and the TNF receptor superfamily member CD40. In mouse models of checkpoint inhibitor–resistant pancreatic cancer, coactivation of Dectin-1, via systemic β-glucan therapy, and CD40, with agonist antibody treatment, eradicated established tumors and induced immunological memory. Antitumor activity was dependent on cDC1s and T cells but did not require classical T cell–mediated cytotoxicity or blockade of checkpoint molecules. Rather, targeting CD40 drove T cell–mediated IFN-γ signaling, which converged with Dectin-1 activation to program distinct macrophage subsets to facilitate tumor responses. Thus, productive cancer immune surveillance in pancreatic tumors resistant to checkpoint inhibition can be invoked by coactivation of complementary myeloid signaling pathways.

INTRODUCTION

Therapies aimed at leveraging the cytotoxic potential of T cells [e.g., immune checkpoint blockade (ICB) and chimeric antigen receptor T cell therapy] have revolutionized cancer treatment (*1*). However, many tumor histologies are profoundly resistant to T cell immunosurveillance (*2*–*4*). One key determinant of outcomes to T cell–targeted immunotherapy is the immune composition of the tumor microenvironment (TME) (*5*). The TME of T cell immunotherapy–resistant tumors typically lacks T cells and demonstrates extensive myeloid inflammation, consisting of granulocytes, macrophages, and monocytes (*5*–*8*).

Myeloid cells commonly undermine productive immunosurveillance in cancer via suppression of T cell responses (*9*). However, myeloid cells are crucial first responders to invading microbes/tissue injury and thus are endowed with immunostimulatory functionality (*10*). Furthermore, intratumoral myeloid cells are pliable and, despite immunosuppressive programming, maintain the capacity for T cell priming, phagocytosis, and production of tumoricidal factors (*11*, *12*). Thus, immune-resistant tumors are not necessarily immunologically inert, because they can contain myeloid cells capable of performing antitumor functions. Together, these observations prompted us to consider whether activating the myeloid infiltrate could reveal a therapeutic vulnerability in otherwise immune-resistant tumors.

Key challenges that have yet to be overcome for successful targeting of myeloid cells in cancer include (i) avoiding activation of compensatory immunosuppressive myeloid pathways that emerge upon targeting a single myeloid population/pathway and (ii) maintaining the immunostimulatory capacity of myeloid cells that can be inadvertently suppressed or reduced by blocking or depleting treatments (*13*, *14*). Here, we found that cotargeting of dual myeloid-activating pathways was synergistic, driving tumor eradication and immunological memory against ICB-resistant cancer. We showed that treatment with an agonist against the tumor necrosis factor (TNF) receptor superfamily member CD40 in combination with a soluble β-glucan (BG), which targets the C-type lectin receptor (CLR) Dectin-1, was sufficient to trigger productive immunosurveillance in ICB-resistant mouse models of pancreatic ductal adenocarcinoma. Underlying antitumor activity, CD40 agonist–induced interferon-γ (IFN-γ)–signal transducer and activator of transcription 1 (STAT1) signaling and Dectin-1 activation combined to drive antitumor effector myeloid responses, bypassing the need for classical T cell cytolytic mechanisms [e.g., perforin and tumor major histocompatibility complex (MHC) expression] or blockade of T cell immune checkpoints. Together, our results identify a cancer immunotherapy strategy in which activation of complementary myeloid signaling pathways is sufficient to enforce productive immunosurveillance in murine pancreatic cancer.

RESULTS

Intratumoral myeloid cells in pancreatic ductal adenocarcinoma express activating receptors

Pancreatic ductal adenocarcinoma (PDA) is a prototype of myeloid inflammation and resistance to T cell immunotherapy (*15*). Therefore, we first analyzed publicly available single-cell RNA sequencing (scRNA-seq) (*16*) generated from human PDA tumors. We computationally sorted myeloid cells (7763 total cells; Fig. 1A and fig. S1A) and assessed expression of putative myeloid-activating receptors, including TNF receptor (TNFR) superfamily members and pattern recognition receptors (PRRs) (Fig. 1, B to C). Among the

[1]Division of Hematology and Oncology, Department of Medicine, Perelman School of Medicine, University of Pennsylvania, Philadelphia, PA, USA. [2]Abramson Cancer Center, Perelman School of Medicine, University of Pennsylvania, Philadelphia, PA, USA. [3]HiberCell Inc., Roseville, MN, USA.
*Corresponding author. Email: gregory.beatty@pennmedicine.upenn.edu (G.L.B); max.wattenberg@pennmedicine.upenn.edu (M.M.W.)
†Present address: GlaxoSmithKline, Upper Providence, PA, USA.

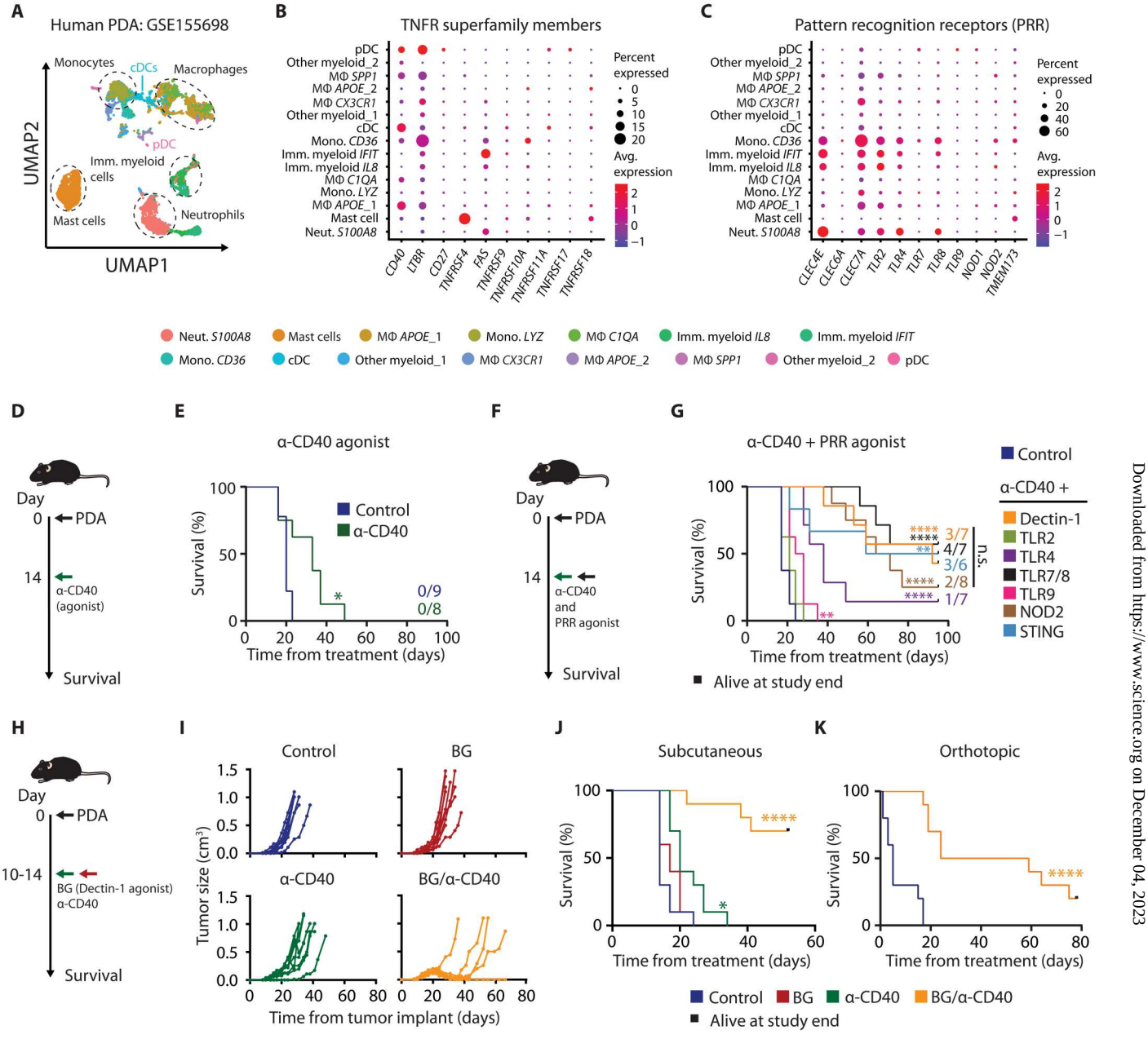

Fig. 1. Combined activation of myeloid receptors promotes synergistic cancer therapy in pancreatic ductal adenocarcinoma. (**A**) UMAP plot of myeloid cells in human PDA ($n = 16$). (**B**) Dot plot of TNFR superfamily member and (**C**) PRR gene expression in myeloid cells from human PDA ($n = 16$). *CLEC7A* encodes for Dectin-1. (**D**) Study schema showing mice ($n = 8$ or 9 per group) injected subcutaneously with PDA.7940B and treated with aCD40. (**E**) Kaplan-Meier survival analysis of (D). Numbers indicate mice remaining alive at study end. (**F**) Study schema showing mice ($n = 6$ to 8 per group) injected subcutaneously with PDA.7940B and treated with aCD40 plus systemic administration of the indicated PRR agonist. (**G**) Kaplan-Meier survival analysis of (F). Numbers indicate mice remaining alive at study end. (**H**) Study schema showing mice with subcutaneous or orthotopic PDA.7940B tumors and treated with aCD40 [0.1 mg intraperitoneally (i.p.)], BG [1.2 mg intravenous (i.v.)], or the combination. (**I**) Tumor volume over time. (**J**) Kaplan-Meier survival analysis of mice ($n = 10$ per group) treated as in (H). (**K**) Kaplan-Meier survival analysis of mice ($n = 10$ per group) with orthotopic pancreas tumors. Log-rank tests were used (E, G, J, and K) for pairwise comparison among all groups. Asterisks represent significance testing compared with control. $^*P < 0.05$, $^{**}P < 0.01$, and $^{****}P < 0.0001$. (E) to (K) are representative of two independent experiments.

most abundantly expressed TNFRs was *CD40*, which has been studied for its capacity to stimulate macrophage and dendritic cell (DC) subsets (*17*, *18*). Clinical-grade monoclonal antibodies with agonist activity against CD40 induce on-target biological activity in patients (*19*) yet thus far show limited clinical activity in early-phase clinical trials (*20*, *21*). We hypothesized that combined activation of CD40 and a second myeloid signaling pathway might trigger a more effective antitumor immune response.

Myeloid clusters also expressed PRRs, which function to recognize pathogen-associated molecular patterns (*22*). PRRs expressed by intratumoral myeloid clusters included CLRs, Toll-like receptors (TLRs), nucleotide oligomerization domain (NOD) receptors, and stimulator of interferon genes (STING; Fig. 1C). PRRs were frequently expressed by macrophage, monocyte, and granulocyte clusters that lacked robust *CD40* expression. Additional analysis of scRNA-seq from human glioblastoma, microsatellite stable colorectal cancer liver metastases, and head and neck squamous cell carcinoma (*23*–*25*) showed similar myeloid cell expression of TNFR superfamily members and PRRs, as observed in PDA, suggesting generalizability of targets across diverse cancer types (fig. S1, B to J). Together, these data suggest that CD40 and PRRs could be rational targets for myeloid activation in cancer.

Combined activation of myeloid receptors eradicates pancreatic tumors in mice

Using ICB-resistant *Kras* and *p53*-driven mouse models of PDA (*26*), we next investigated the antitumor activity of combinatory myeloid pathway activation. Whereas treatment with an anti-mouse CD40 antibody with agonist activity (aCD40) mediated only transient tumor control (Fig. 1, D and E, and fig. S2A), systemic administration of a TLR7/8, STING, NOD2, or Dectin-1 (encoded by the *CLEC7A* gene) agonist in combination with aCD40 led to high rates of tumor cures and triggered immunological memory (Fig. 1, F and G, fig. S2, B and C). However, not all PRRs were efficacious, with transient or minimal antitumor activity seen with aCD40 combined with agonists of TLR2, TLR4, and TLR9.

To further define the mechanistic underpinnings and clinical relevance of myeloid activating therapy, we focused on targeting Dectin-1 (also called CLEC7A), a receptor for β-glucans (BGs), in combination with aCD40 (*27*). Unlike TLR7/8, NOD2, and STING, which are currently targeted using intratumoral approaches, BG can be delivered systemically in humans without significant toxicity (*28*). BG showed modest clinical activity in combination with chemotherapy in patients with cancer (*29*) and limited activity as monotherapy in mouse models of PDA (Fig. 1, H and I). However, BG combined with aCD40 showed synergy with marked tumor control in subcutaneous and orthotopic models of PDA and against two distinct mouse PDA tumor cell lines (Fig. 1, H to K, and fig. S2, D and E). In addition, combination treatment showed no evidence of increased rates of cytokine release syndrome or hepatotoxicity (*30*), which are common adverse events with aCD40 (fig. S2, F and G). Together, these results indicate that combinatory activation of myeloid signaling pathways can drive potent antitumor immunity without triggering dose-limiting toxicity in mouse models of PDA.

Myeloid agonists drive distinct intratumoral immune landscapes

We next used mass cytometry (CyTOF) and dimensionality reduction with uniform manifold approximation and projection (UMAP) analyses of orthotopic tumors to gain insight into the cellular mechanisms underlying the activity of combined myeloid agonist therapy (Fig. 2A and fig. S3A). scRNA-seq analysis of untreated pancreatic orthotopic tumors showed similar immune composition to that of autochthonous mouse models of PDA, based on comparison with publicly available data (fig. S3B) (*31*). Evaluation of $CD45^+$ leukocytes in orthotopic tumors at 10 days after BG, aCD40, or the combination identified broad remodeling of intratumoral myeloid and lymphoid cells (Fig. 2, B and C). Focusing first on the myeloid compartment, we integrated the frequencies of all myeloid clusters and identified distinct intratumoral myeloid landscapes to associate with each treatment alone or in combination (Fig. 2, D and E, and fig. S3, C and D). Underlying these changes, BG drove increased frequencies of programmed cell death 1 ligand 1 $(PD\text{-}L1)^{neg}Ly6G^+$ granulocytes (M6) and $CD206^{low}F4/80^+$ macrophages (M7), whereas aCD40 was associated with increased frequencies of inflammatory monocytes (M4) and $IA/IE^+F4/80^+$ macrophages (M5) (Fig. 2F and fig. S3, D and E). Combination therapy triggered similar changes as seen after BG or aCD40 monotherapy, as well as specific changes, such as a significant decrease in $CD206^+PD\text{-}L1^+$ macrophages (M8; Fig. 2F and fig. S3E). $CD206^+$ marks a prototypical immunosuppressive macrophage subset (*32*), suggesting that treatment shifted tumor-associated macrophages (TAMs) away from a tumor-promoting state. Together, these data show that distinct changes in intratumoral myeloid composition can be triggered by the activation of distinct myeloid signaling pathways.

We also performed dimensionality reduction analysis of intratumoral T cells, which revealed a major impact of aCD40 treatment, and not BG, on T cell composition (Fig. 2, G and H, and fig. S3, F and G). aCD40 treatment with or without BG increased the frequency of $CD4^+$ T cells expressing Ki67, inducible T cell costimulator (ICOS), and CD127 (L1) and $CD8^+$ T cells with low expression of immunoregulatory molecules, including programmed cell death 1 (PD-1), cytotoxic T lymphocyte–associated protein 4 (CTLA-4), lymphocyte activation gene 3 (LAG3), and T cell immunoglobulin receptor and mucin domain–containing protein 3 (Tim3) (L2) (Fig. 2I and fig. S3, G and H). Treatment with aCD40 also reduced the frequency of several T cell clusters, including $Foxp3^+$ regulatory T cells (L6). These data suggest that CD40 activation is a major driver of T cell biology in the context of combined myeloid-activating therapy.

We next investigated the molecular underpinnings of the identified cellular changes using bulk RNA-seq of tumors. As with cellular populations, broad transcriptional remodeling after treatment was seen, related to both BG and aCD40 (fig. S4, A to C). Gene set enrichment analysis showed that BG with or without aCD40 triggered innate immune activation, cytokine production, and myeloid migration pathways (Fig. 2, J and K, and fig. S4D). Hence, BG treatment drove increased myeloid-recruiting chemokine expression (*Cxcl2*, *Cxcl3*, and *Ccl2*). This suggested that up-regulation of chemokine axes mediated the observed increases in granulocytes and macrophages with BG. In contrast, aCD40 with or without BG primarily drove pathways supportive of lymphocyte and T cell activation, as evidenced by up-regulation of T cell

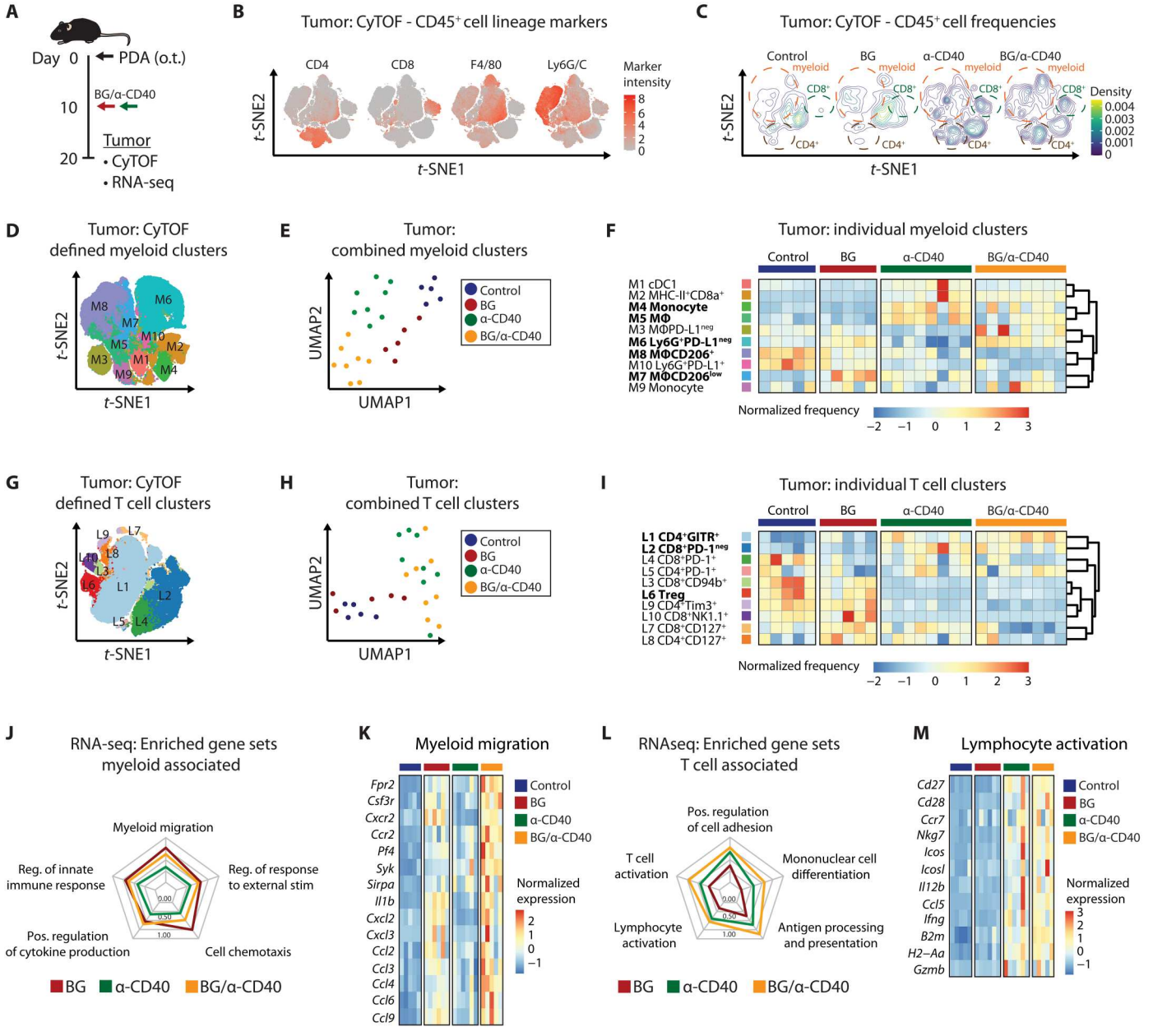

Fig. 2. Myeloid-targeting therapy drives distinct tumor immune landscapes. (**A**) Study schema. (**B**) *t*-SNE plots of selected lineage markers. (**C**) Density plots. (**D**) *t*-SNE showing FlowSOM-defined myeloid clusters. (**E**) UMAP projection. Each dot is an individual mouse tumor defined by the relative frequencies of $n = 10$ CyTOF-defined myeloid cell clusters in control ($n = 5$) mice and mice treated with BG ($n = 5$), aCD40 ($n = 8$), and BG/aCD40 ($n = 8$). (**F**) Heatmap of myeloid clusters. Bolded text indicates selected clusters significantly altered by BG, aCD40, or BG/aCD40 treatment as compared with control. Significance testing performed using one-way ANOVA with Tukey's and displayed in fig. S3E. Columns represent biological replicates. (**G**) *t*-SNE of FlowSOM-defined T cell clusters. (**H**) UMAP projection. Each dot is an individual mouse tumor defined by the relative frequencies of $n = 10$ CyTOF-defined T cell clusters in control ($n = 5$) mice and mice treated with BG ($n = 5$), aCD40 ($n = 8$), and BG/aCD40 ($n = 8$). (**I**) Heatmap of T cell clusters. Bolded text indicates clusters significantly altered by aCD40 or BG/aCD40 treatment as compared with control. Significance testing was performed using one-way ANOVA with Tukey's test and is displayed in fig. S3H. Columns represent biological replicates. (**J**) Radar plot of selected myeloid-related GSEA pathways based on bulk RNA-seq of tumors from control ($n = 5$) mice and mice treated with BG ($n = 6$), aCD40 ($n = 6$), and BG/aCD40 ($n = 5$). Axis is normalized enrichment score relative to a range of 1.5 to 2.2. (**K**) Heatmap of selected genes related to myeloid migration gene set. (**L**) Radar plot of selected T cell–related GSEA pathways. Axis and experimental approach is as in (J). (**M**) Heatmap of selected genes related to lymphocyte activation gene set.

differentiation/activation genes (*Cd27*, *Cd28*, and *Icos*), T cell–supporting cytokines (*Il12b* and *Il15*), and antigen presentation genes (*B2m* and *H2-Aa*; Fig. 2, L and M, and fig. S4E). In total, these cellular and transcriptional data demonstrate that activation of BG therapy drives innate immune programs and that aCD40 triggers innate and adaptive immunity, yet only targeting of both myeloid signaling pathways together is associated with productive immunosurveillance.

Antitumor activity of myeloid agonist therapy is independent of T cell immune checkpoints

Transcriptional analysis also identified up-regulation of the *Pdcd1*, *Cd274* (which encodes PD-L1), and *Ctla4* immune checkpoints (Fig. 3A). This prompted us to study whether myeloid activation might combine with ICB to further improve responses. As expected, mouse models of PDA were resistant to dual blockade of PD-1 (aPD-1) and CTLA-4 (aCTLA-4; Fig. 3, B and C, and fig. S4F), consistent with the clinical phenotype of PDA (*2*). However, unexpectedly, the efficacy of BG/aCD40 was not improved upon with the addition of dual ICB or dual ICB plus standard-of-care chemotherapy gemcitabine with nab-paclitaxel (Fig. 3D and fig. S4G) (*33*). We also tested the therapeutic potential of BG/aCD40 with or without aPD-1 in a model of surgically resectable PDA (fig. S5A). Surgery with neoadjuvant or adjuvant therapy is a common treatment paradigm for patients with localized solid tumors, yet relapse is common (*34*, *35*). BG/aCD40/aPD1 administered in the neoadjuvant setting produced pathologic responses and neoadjuvant and adjuvant treatment prolonged survival as compared with surgery alone (fig. S5, B to D). However, aPD-1 and surgery were dispensable for the antitumor activity of BG/aCD40 (Fig. 3, E and F, and fig. S5, E to H). Together, these data demonstrate that combinatorial activation of myeloid signaling pathways can drive deep and durable tumor responses independent of ICB and standard-of-care treatments including chemotherapy and surgery.

T cells and cDC1s are required for antitumor activity

Given that ICB did not enhance the antitumor activity of BG/aCD40, we next investigated whether T cells were necessary for tumor control. Depletion of $CD4^+$ and $CD8^+$ T cells abrogated treatment effectiveness, whereas $CD4^+$ or $CD8^+$ T cell depletion was associated with a partial decrease in tumor control (Fig. 4, A and B, and fig. S5, I to L). In addition, cured mice showed T cell–dependent

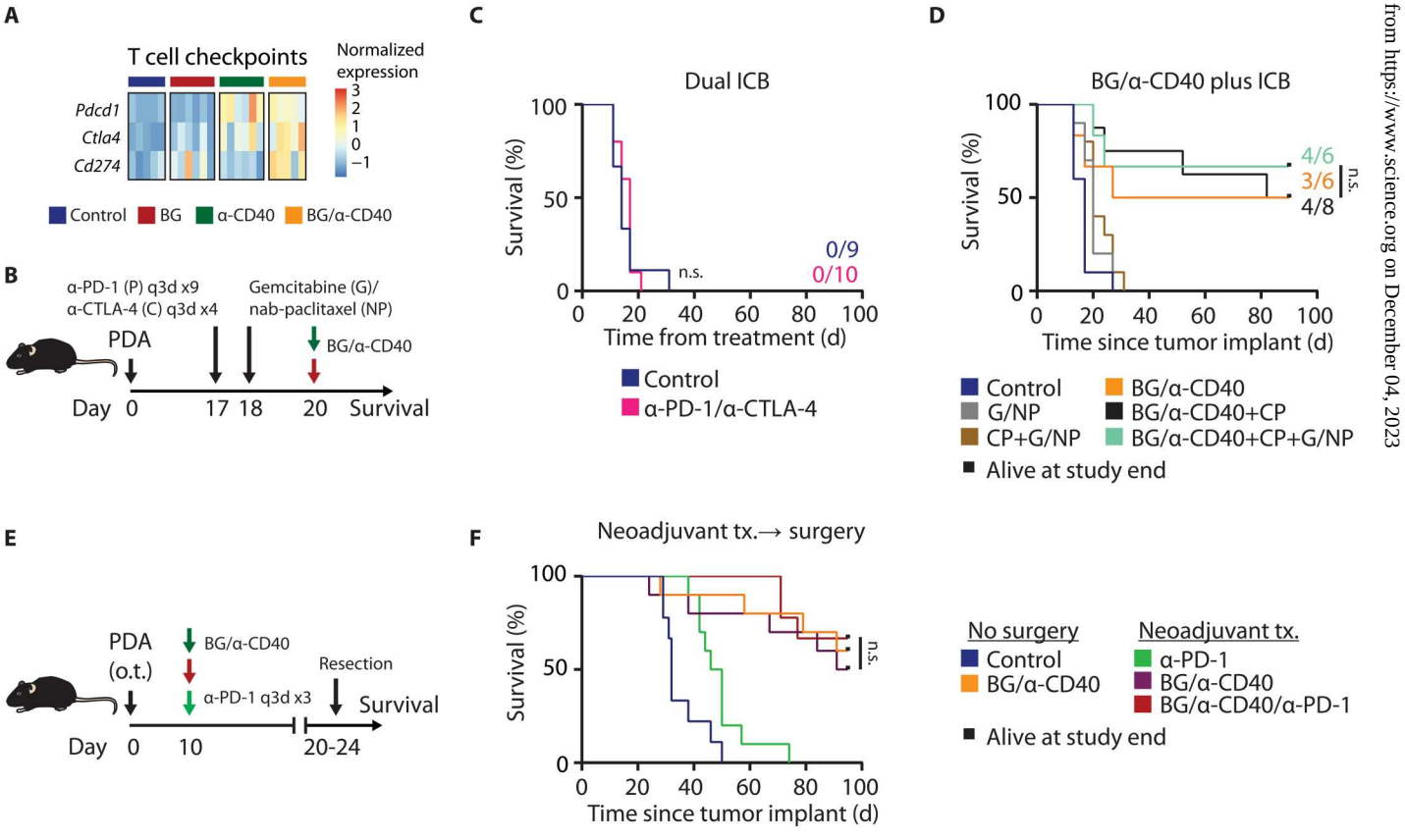

Fig. 3. Antitumor activity of myeloid agonist therapy is independent of T cell immune checkpoints. (**A**) Heatmap of selected genes related to T cell checkpoint molecules. (**B**) Study schema of mice injected subcutaneously with PDA.7940B. (**C**) Kaplan-Meier survival analysis of mice ($n = 9$ or 10 per group) treated with anti–PD-1 plus anti–CTLA-4. Numbers indicate mice remaining alive at study end out of the total treatment cohort. (**D**) Kaplan-Meier survival analysis of mice ($n = 6$ to 8 per group) treated with combinations of gemcitabine plus nab-paclitaxel, anti–PD-1 plus anti–CTLA-4 and BG/aCD40. (**E**) Neoadjuvant treatment study schema. (**F**) Kaplan-Meier survival analysis of (E) with $n = 9$ or 10 mice per group. Log-rank tests were used (C, D, and F) for pairwise comparison among treatment groups. Significance testing indicates comparison of anti–PD-1 plus anti–CTLA-4 versus control (C) or BG/aCD40 versus BG/aCD40 plus the indicated additional therapies (D and F). (B) to (F) are representative of two independent experiments.

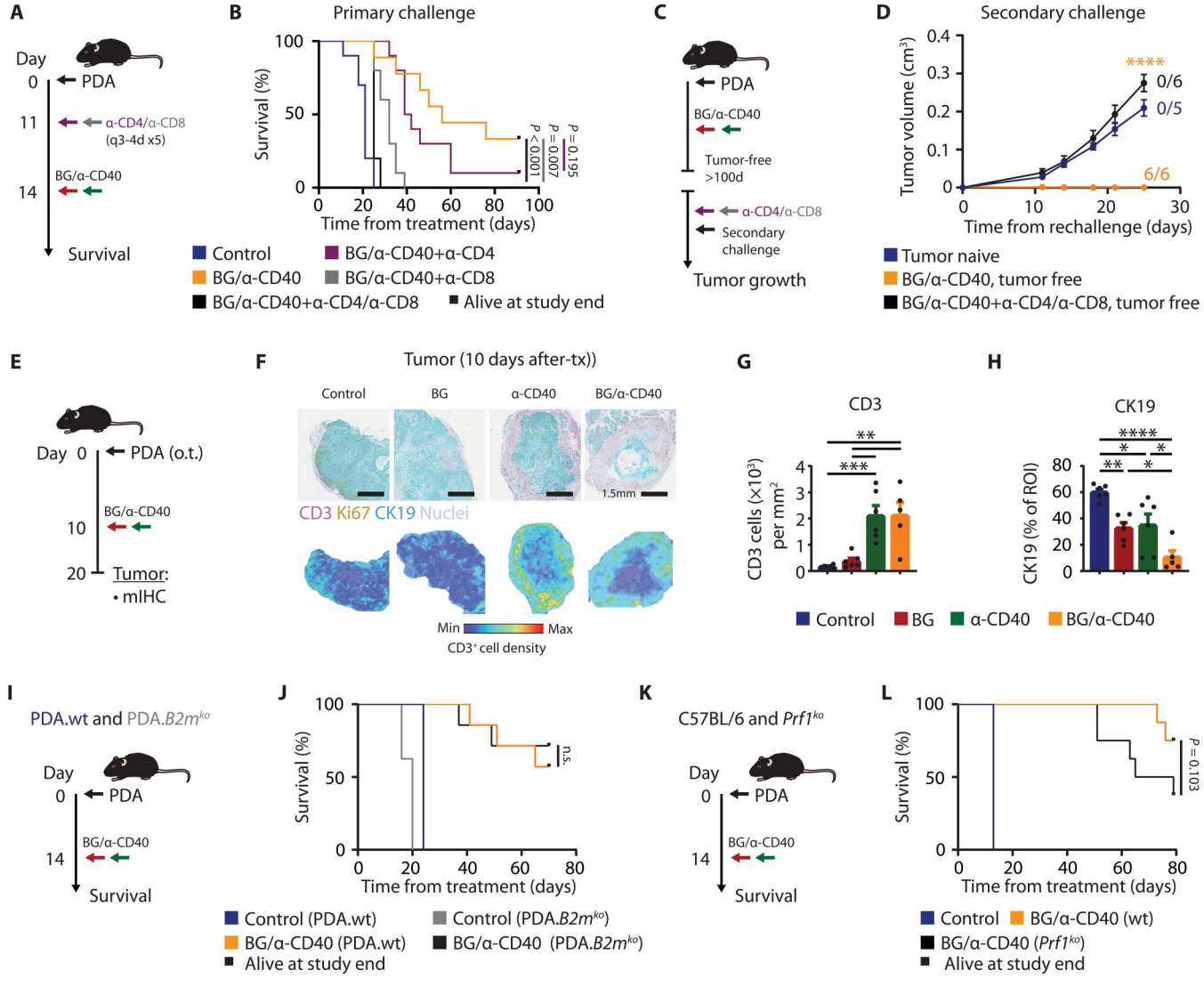

Fig. 4. Classical cytotoxicity pathways are not required for T cell immunosurveillance with myeloid agonist therapy. (**A**) Study schema of mice (n = 9 or 10 per group) injected subcutaneously with PDA.69. (**B**) Kaplan-Meier survival analysis of (A). (**C**) Study schema of secondary tumor challenge. (**D**) Tumor volume over time. Numbers indicate tumor-free mice at end of study. Two-way ANOVA with Tukey's test was used. (**E**) Study schema of mice with PDA.7940B orthotopic pancreatic tumors. (**F**) Representative images of tumors stained for CD3 (purple), Ki67 (yellow), CK19 (teal), and nuclei (blue, hematoxylin) (top). Heatmaps showing density of $CD3^+$ cells (bottom). (**G**) Quantification of $CD3^+$ cells per mm^2 in control and BG-, aCD40-, and BG/aCD40-treated mice (n = 5 or 6 per group). (**H**) Quantification of CK19 percentage of tumor region in control and BG-, aCD40-. and BG/aCD40-treated mice (n = 5 or 6 per group). One-way ANOVA with Tukey's test was used in (G) and (H). (**I**) Study schema. (**J**) Kaplan-Meier survival analysis of (I) with n = 7 or 8 per group. (**K**) Study schema. (**L**) Kaplan-Meier survival analysis with n = 8 per group. Log-rank tests were used (B, J, and L) for pairwise comparison among all groups. Displayed significance testing indicates BG/aCD40 compared with the indicated treatment group. Data are shown as mean ± SEM; *P < 0.05, **P < 0.01, ***P < 0.001, and ****P < 0.0001. (A) to (L) are representative of at least two independent experiments.

immunological memory upon secondary tumor challenge (Fig. 4, C and D, and fig. S5, M and N). Antitumor immunity triggered by aCD40 when combined with ICB or chemotherapy is dependent on type 1 cDCs (cDC1) (*36*, *37*). Consistent with this, tumor responses were significantly diminished, and durable control lost, in cDC1-deficient *Batf3*^{ko} mice treated with BG/aCD40 (fig. S6, A to C). Furthermore, tumor infiltration by $CD4^+$ and $CD8^+$ T cells, as well as T cell proliferation (measured by Ki67) in the peripheral blood, was significantly decreased in *Batf3*^{ko} mice as compared with wild-type controls (fig. S6, D to F). These results show that T cells are required for antitumor activity with BG/aCD40 therapy and that T cell activation and recruitment are mediated by cDC1s.

Both Dectin-1 and CD40 have been implicated in enhancing T cell priming (*37*, *38*), and we reasoned that combination therapy might be augmenting cDC function. However, although BG bound Dectin-1–expressing cDCs type 2 (cDC2) and, to a lesser extent, cDC1s, the combination of BG and aCD40 only modestly increased the expression of costimulatory molecules (CD40, CD80, and CD86) on lymph node and splenic cDCs beyond that achieved by aCD40 alone (fig. S6, G to K). Furthermore, immunohistochemistry (IHC) analysis demonstrated that increased T cell

infiltration into tumors was driven solely by aCD40 without a contribution of BG (Fig. 4, E to G). T cell infiltration was not sufficient to trigger eradication because only BG and CD40 treatment drove a near-complete elimination of CK19$^+$ tumor cells and decreased tumor cell proliferation despite marked increases in T cell infiltration with aCD40 monotherapy (Fig. 4H and fig. S7, A and B). In sum, these data support that aCD40 and not BG is the major driver of cDC1-mediated T cell activation, which is necessary but not sufficient for effective tumor control.

Canonical T cell cytotoxicity pathways are not required for antitumor activity

We next sought to define the mechanistic contribution of T cells to antitumor immunity induced by BG/aCD40. Spatial analysis of the TME showed that the majority of T cells surrounded but did not invade tumor lesions after aCD40 with or without BG (Fig. 4F). This finding suggested that T cells may not be acting to kill tumor cells via canonical perforin/granzyme cytotoxicity, which requires direct T cell–tumor cell interactions via T cell receptor (TCR)–peptide/MHC (pMHC) binding (*39*). Mouse PDA tumor cells knocked out for MHC class I via CRISPR-Cas9 editing of *B2m*, and which lacked MHC class II, remained responsive to BG/aCD40 therapy (Fig. 4, I and J, and fig. S7, C to F). Moreover, activity of BG/aCD40 also persisted in *Prf1*^{ko} mice, which display deficits in T cell– and natural killer (NK) cell–mediated lysis due to absent expression of perforin (*40*) (Fig. 4, K and L, and fig. S7G). These data demonstrate that although T cells are required for antitumor activity, they are not acting as cytotoxic effectors.

IFN-γ is sufficient to enforce antitumor activity of Dectin-1 activation

We next investigated the molecular contributions of intratumoral T cells to the antitumor response using scRNA-seq analysis of orthotopic tumors (22,706 total cells) at 8 days after treatment (Fig. 5A and fig. S8, A to C). Computational sorting of lymphoid cells identified 13 populations, including NK cells, NKT cells, type 2 innate lymphoid cells (ILC2s), B cells, plasma cells, rare gamma-delta (γδ) T cells, and alpha-beta (α/β) T cells (Fig. 5A and fig. S8D). Consistent with CyTOF and RNA-seq data, the major treatment-related changes in the lymphoid compartment were of T cells and were driven by aCD40 with or without BG. To this end, aCD40 was associated with decreased regulatory T cells and increased CD4$^+$ *Tcf7*- and CD4$^+$ *Tox*-expressing T cell clusters (Fig. 5B). In addition, aCD40 or BG/aCD40 transcriptionally activated and increased the frequency of CD8$^+$ *Cxcr6* T cells, a stem-like population, which accumulates in tumor stromal niches (*41*), and CD8$^+$ *Cx3cr1* T cells, a tumor-specific effector memory-like population (*42*). In agreement with this, CD8$^+$ *Cxcr6* and CD8$^+$ *Cx3cr1* T cell clusters were putative tumor antigen–specific T cells based on enrichment in a 50-gene tumor-specific T cell gene set (fig. S8E) (*43*).

A major function of T cells is tumor cell killing via classical contact-dependent cytotoxicity pathways, yet in the context of

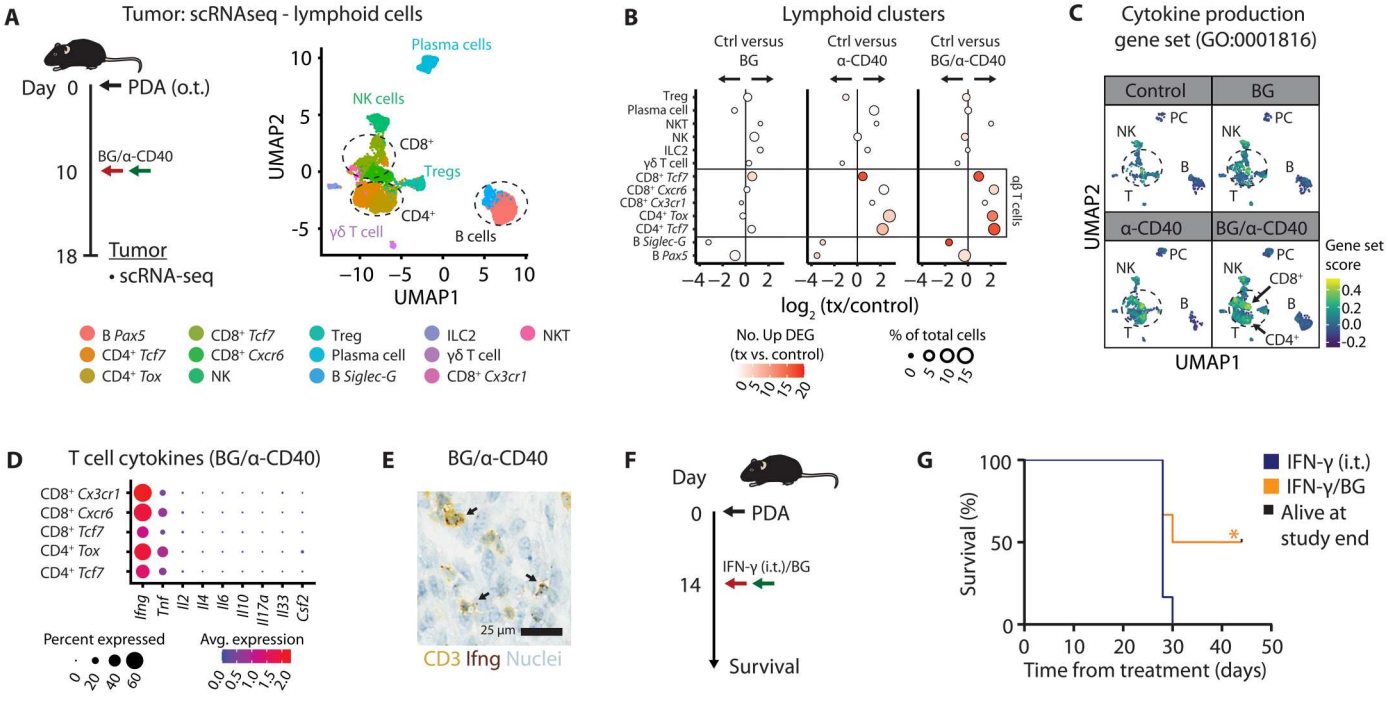

Fig. 5. IFN-γ is expressed by T cells and enforces the antitumor activity of Dectin-1–targeted therapy. (**A**) Study schema (left) and UMAP projection of computationally sorted lymphoid cells defined by scRNA-seq (right). Two samples (each consisting of two or three pooled tumors) per treatment condition were analyzed. (**B**) Dot plot of relative change in frequency of lymphoid populations comparing treatment with control. Values are $\log_2$ fold change. Size represents the percentage of the population of total cells in each condition. Color represents the number of up-regulated DEGs in the indicated treatment versus control. (**C**) Gene set score of Regulation of Cytokine Production (GO:0001816) gene set. PC, plasma cell; B, B cell; NK, NK cell. (**D**) Dot plot of selected cytokines in T cells from BG/aCD40-treated tumors. (**E**) IHC for CD3 (yellow) and nuclei (blue, hematoxylin) and RNA in situ hybridization for *Ifng* (brown). Arrows highlight CD3$^+$*Ifng*$^+$ cells. (**F**) Study schema. (**G**) Kaplan-Meier survival analysis of (F) in mice treated with intratumoral (i.t.) IFN-γ (n = 6) or IFN-γ/BG. Log-rank test was used. *P < 0.05. (F) to (G) are representative of two independent experiments.

BG/aCD40, tumor MHC expression was not required for efficacy. Consistent with this, T cell clusters affected by aCD40 did not show up-regulation of a T cell cytotoxicity gene set (fig. S8F). In contrast, genes associated with positive regulation of cytokine production were highly expressed in $CD4^+$ and $CD8^+$ T cell subsets after aCD40 or BG/aCD40 (Fig. 5C). Further analysis identified *Ifng* to be among the most highly expressed cytokines by T cells in BG/aCD40-treated tumors (Fig. 5, D and E). *Ifng* expression was restricted to $CD4^+$ and $CD8^+$ T cells and a rare NK cell population (fig. S8G). IFN-γ is a multifunctional cytokine, which can reprogram myeloid cells and directly affect tumor cells (*44*). Intratumoral administration of mouse recombinant IFN-γ, in the absence of CD40 activation, was sufficient to enforce the antitumor activity of BG therapy, prolonging survival in BG-resistant mouse models of PDA (Fig. 5, F and G). Overall, these data suggest that aCD40 drives T cell infiltration and production of IFN-γ, which combines with BG therapy to mediate antitumor immunity.

Host Dectin-1 is necessary for antitumor activity

Having established the major determinants of antitumor activity associated with CD40 activation, we next aimed to define the role of the BG receptor Dectin-1. Profiling of tumor-infiltrating leukocytes in untreated mouse PDA tumors showed a similar pattern of Dectin-1 expression as that seen in human solid tumors. Dectin-1 was expressed by $Ly6C^+$ monocytes and $F4/80^+$ TAMs, as well as $CD11c^+$ DCs and $CD19^+$ B cells and, at lower levels, $Ly6G^+$ cells (fig. S9, A to E). In addition, we assessed the binding of BG to intratumoral immune cells by treating wild-type and *Clec7a*^{ko} mice bearing pancreatic orthotopic tumors with fluorescently labeled BG (BG-DTAF). Dectin-1 expression and Dectin-1–dependent binding of BG by intratumoral immune cells were discordant, suggesting selective biodistribution of BG. Flow cytometry showed that most Dectin-1–dependent binding of BG at 18 hours after treatment was to $Ly6C^{hi}$ monocytes and $Ly6G^+$ granulocytes but not $F4/80^+$ TAMs, T or B lymphocytes, or CD45-negative cells (tumor cells and fibroblasts; Fig. 6A and fig. S9, F and G). Despite B cell expression of Dectin-1 and BG binding to $Ly6G^+$ cells, these cell types did not play a major role in the antitumor response because treatment with mouse anti-CD20 or anti-Ly6G depleting antibodies had no significant impact on survival in tumor-bearing mice treated with BG/aCD40 (fig. S9, H to K). These data suggest that monocytes are a major target of BG therapy. Monocytes differentiate into TAMs in the TME, and consistent with this, scRNA-seq analysis using pseudotime, a measure of a transition through differentiation, demonstrated an increase from monocytes to TAMs in BG/aCD40-treated tumors (fig. S9L). Functionally, Dectin-1 was required for antitumor activity, because suppression of tumor growth and prolonged survival driven by BG/aCD40 was not seen in *Clec7a*^{ko} mice (Fig. 6, B and C, and fig. S9M). Furthermore, tumors obtained from BG/aCD40-treated wild-type mice, but not *Clec7a*^{ko} mice, showed a significant increase in TAM–to–tumor cell ratio as compared with untreated mice (Fig. 6, D and E), supporting a role for Dectin-1 signaling in remodeling the TME and potentially affecting TAM biology.

Antitumor activity is independent of tumor-intrinsic IFN-γ signaling

Having identified a potential role for BG in targeting monocytes and TAMs, we next investigated how CD40 activation might converge with this biology to trigger cancer immunosurveillance. We first evaluated for evidence of IFN-γ–responsive cells in the TME. IHC analysis of tumors showed robust activation of the IFN-γ signaling pathway member STAT1 (measured by p-STAT1^{Tyr701}) in $CK19^+$ tumor cells and $CK19^{neg}$ stromal cells, associated with aCD40 treatment (fig. S10, A and B). IFN-γ can directly affect tumor cells, inducing senescence and apoptosis (*45*). However, BG/aCD40 treatment triggered similarly deep responses against wild-type and mouse PDA tumor cells CRISPR-Cas9–edited with knockout of IFN-γR1 (fig. S10, C to F). These findings suggest that stromal cells are the primary target of IFN-γ and might contribute to antitumor activity of BG/aCD40.

Transcriptional programming of TAMs

Analysis of nontumor cells within the TME identified $F4/80^+$ TAMs to be a major contributor to the stromal compartment both within (intratumoral) and bordering (border) tumor lesions (Fig. 7A). Furthermore, the combination of BG/aCD40 led to a significant increase in intratumoral TAMs by 10 days after treatment (Fig. 7B),

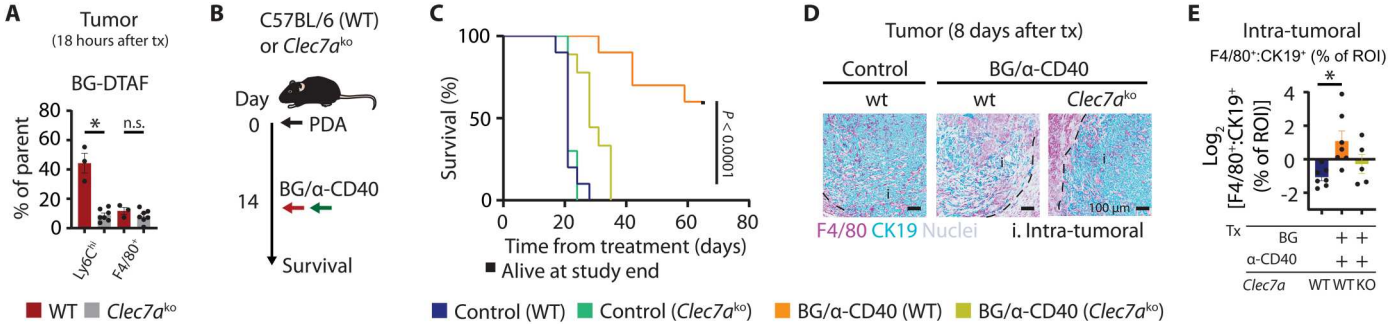

Fig. 6. Host Dectin-1 is required for antitumor activity of myeloid activating therapy. (**A**) Quantification of BG-DTAF expression 18 hours after treatment in WT ($n = 3$) and *Clec7a*^{ko} ($n = 7$) mice. Mann-Whitney *U* tests were performed. (**B**) Study schema in mice implanted subcutaneously with PDA.7940B tumors. (**C**) Kaplan-Meier analysis of (B) with $n = 9$ or 10 mice per group. Log-rank test was used for pairwise comparison among all groups. Significance testing represents BG/aCD40 (WT) versus BG/aCD40 (*Clec7a*^{ko}). (**D**) Representative IHC of PDA.7940B orthotopic tumor for F4/80 (purple), CK19 (teal), and nuclei (blue, hematoxylin). Dotted line denotes tumor border. (**E**) Quantification of IHC in control WT mice ($n = 7$) and BG/aCD40-treated WT ($n = 7$) and *Clec7a*^{ko} ($n = 5$) mice. Log_2-transformed values are shown. Data represents two combined independent experiments. One-way ANOVA with Tukey's was used. MΦ, macrophage. Data are shown as mean ± SEM; $^*P < 0.05$. (A) to (C) are representative of two independent experiments.

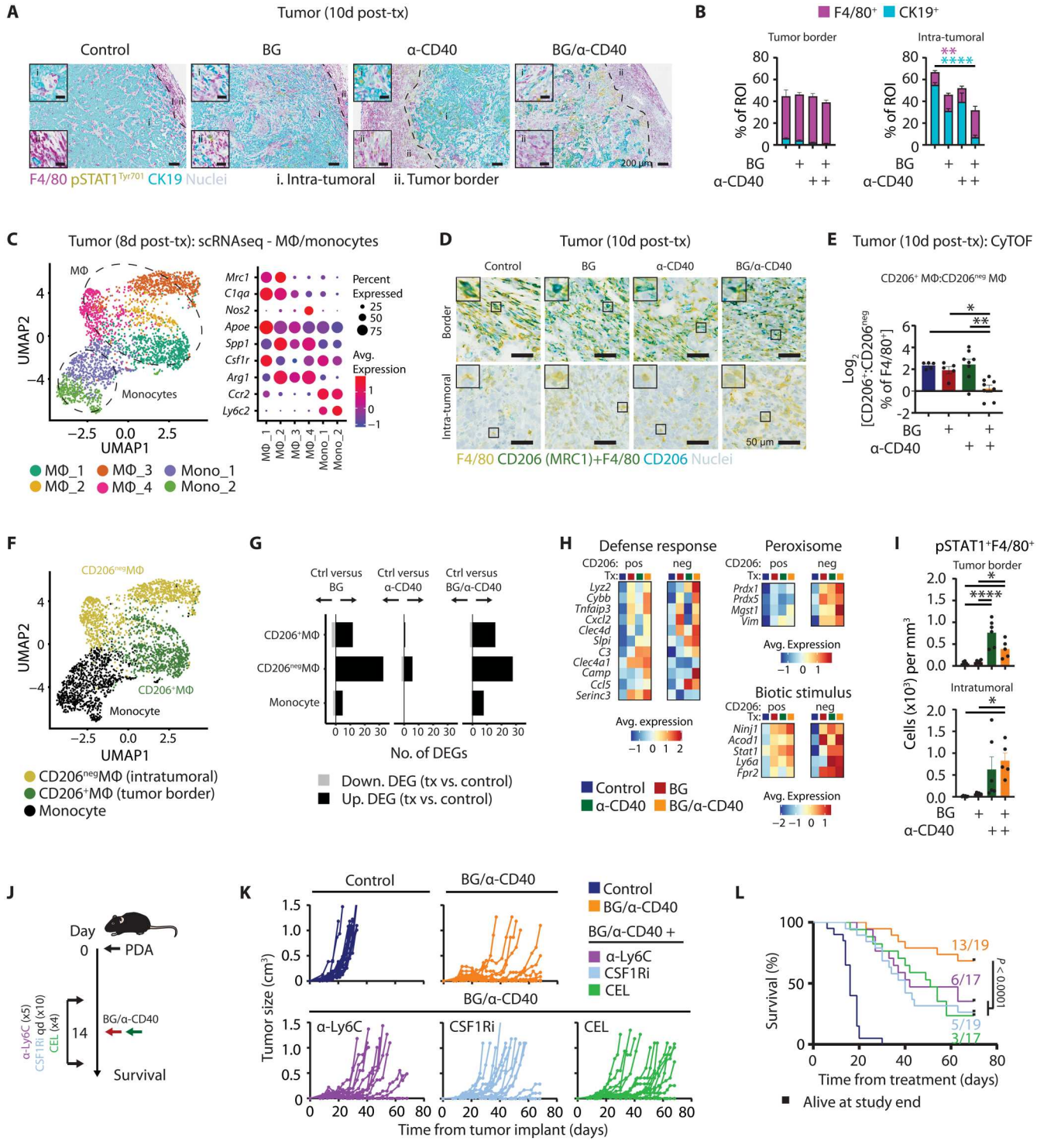

Fig. 7. Targeting Dectin-1 converges with CD40 agonist-driven IFN-γ to program TAMs. (**A**) IHC of orthotopic PDA.7940B tumors 10 days after treatment. (**B**) Quantification of IHC in (A) (n = 5 or 6 mice per group). (**C**) UMAP projection (left) and dot plot (right) of scRNA-seq from orthotopic PDA.7940B tumors. (**D**) IHC of orthotopic PDA.7940B tumors. (**E**) Quantification of $\log_2$ fold change of CyTOF defined CD206$^+$ and CD206^{neg} populations. (**F**) UMAP projection of scRNA-seq–defined monocytes/MΦs. (**G**) Bar graph of DEGs in monocytes/MΦs in treatment versus control. (**H**) Heatmaps of average expression of selected genes significantly up-regulated with BG/aCD40 in CD206$^+$ or CD206^{neg} MΦs compared with control. Columns represent treatment group. (**I**) Quantification of IHC in (A). (**J**) Study schema. (**K**) Tumor growth curves. Data represents two combined independent experiments. (**L**) Kaplan-Meier survival analysis of (J). Log-rank test was used. Significant testing indicates pairwise comparisons between BG/aCD40 and BG/aCD40 plus myeloid cell depletion. Numbers indicate mice remaining alive at study end. One-way ANOVA with Tukey's was used (B, E, and I). Data are shown as mean ± SEM; *P < 0.05, **P < 0.01, ***P < 0.001, and ****P < 0.0001. (A), (B), and (I) to (L) are representative of at least two independent experiments.

suggesting that TAMs may be playing a crucial role in the antitumor response driven by BG/aCD40. Given these findings, we used scRNA-seq and IHC to dissect the molecular and spatial responses of TAM and monocyte subsets to treatment. Computational sorting of scRNA-seq–defined myeloid cells identified four TAM populations and two monocyte populations (Fig. 7C and fig. S10G). Consistent with known TAM phenotypes, the presence or absence of *Mrc1* (which encodes CD206) and *C1qa* coexpression defined two groups of TAMs (Fig. 7C). CD206^{+}C1q^{+} macrophage accumulation in solid tumors is associated with T cell exhaustion and cancer progression (*46*). Spatial characterization of TAM subsets showed that CD206^{+}TAMs populated the tumor border region, whereas CD206^{neg}TAMs were found in the intratumoral region (Fig. 7D). Moreover, CyTOF analysis demonstrated enrichment of immunosuppressive-like CD206^{+}F4/80^{+}TAMs in untreated tumors and a significant decrease in the ratio of CD206^{+} to CD206^{neg}F4/80^{+}TAMs with BG/aCD40 therapy, consistent with an influx of antitumor-like CD206^{neg}TAMs into the intratumoral region (Fig. 7E and fig. S10H). Furthermore, differentially expressed gene (DEG) analysis of TAMs defined by *Mrc1* (*Cd206*) expression identified BG to be the primary driver of TAM transcriptional state at 8 days after treatment, with the greatest impact on *Mrc1*^{neg}TAMs and fewer transcriptional changes in *Mrc1*$^{+}$TAMs and monocytes (Fig. 7, F and G). In addition, *Mrc1*^{neg} and *Mrc1*$^{+}$ TAMs from BG/aCD40-treated tumors showed immunostimulatory transcriptional programs, including defense response and biotic stimulus, whereas only *Mrc1*^{neg} TAMs showed peroxisome activity (Fig. 7H and table S1 and S2). Although BG was the major driver of these pathways, up-regulation of the IFN-γ–responsive genes *Stat1* and *Ly6a* was associated with aCD40 treatment. Furthermore, p-STAT1$^{Tyr701+}$F4/80^{+} TAMs were identified by IHC within both the tumor border and intratumoral regions after aCD40 or aCD40/BG therapy, consistent with TAM reactivity to IFN-γ (Fig. 7, A and I). Together, these data suggest that transcriptional programming of spatially discrete TAMs is mediated by aCD40-associated IFN-γ–STAT1 signaling in combination with BG therapy.

Monocytes and TAMs are required for optimal antitumor activity

Last, we assessed the functional role of monocytes and TAMs in the antitumor response triggered by BG/aCD40. To this end, depletion of Ly6C^{+} cells using anti-Ly6C antibody treatment significantly reduced the efficacy of BG/aCD40 (Fig. 7, J to L), consistent with a Ly6C^{high} monocyte–derived source of immunostimulatory TAMs in PDA (*47*). Furthermore, pharmacologic targeting of CSF1–CSF1R signaling using GW2580 (CSF1Ri) or phagocytic cells using clodronate liposomes (CELs) also significantly reduced survival in mice treated with BG/aCD40 (Fig. 7, J to L). CEL primarily targets phagocytic cells outside the TME, and CSF1Ri targets intratumoral TAMs (*48*). Thus, these data show that systemic phagocytic cells, a potential source of intratumoral TAMs, and CSF1R-dependent TAMs are crucial for optimal antitumor activity. In addition, peripheral blood analysis confirmed the myeloid cell–depleting effects of CSF1Ri, CEL, and anti-Ly6C and showed no impact on CD4^{+} or CD8^{+} T cell activation triggered by BG/aCD40 (fig. S10, I to M). Thus, these pharmacologic agents effectively targeted expected myeloid subsets without disrupting cDC1-mediated T cell activation. Together, these data identify a mechanism by which Dectin-1 and aCD40-associated IFN-γ signaling in monocytes and TAMs drive productive immunosurveillance against T cell immunotherapy–resistant tumors.

DISCUSSION

Prior strategies aimed at targeting the myeloid response to cancer have been limited by compensatory changes in additional immunosuppressive myeloid cell populations and loss of myeloid immunostimulatory functions (*49*). Here, we show that coactivation of myeloid cells using a CD40 agonist (aCD40) combined with PRR agonists synergized to invoke productive immunosurveillance in mouse models of pancreatic cancer. To define the mechanisms and clinical relevance of combinatory myeloid pathway activation, we focused on aCD40 plus BG therapy. At the cellular level, cDC1s, T cells, Ly6C^{+} monocytes, and CSF1R-dependent TAMs were necessary for maximal therapeutic activity triggered by coactivation of CD40 and Dectin-1, whereas B cells and granulocytes were dispensable. Thus, antitumor activity driven by BG and aCD40 treatment relies on distinct contributions from multiple adaptive and innate leukocyte subsets, which converge to establish a concerted immunological response to cancer.

Monotherapy with a CD40 agonist or BG therapy shows only modest antitumor activity in patients with solid tumors (*19*, *29*) and in animal models, which we confirmed in our study. In contrast, coadministration of aCD40 plus BG therapy in ICB-resistant mouse models of PDA was synergistic and triggered tumor eradication, highlighting that targeting multiple distinct myeloid-activating receptors can drive productive immunosurveillance. Furthermore, although BGs can bind multiple CLRs (*27*), in our study, genetic deletion of *Clec7a* in mice abrogated antitumor activity triggered by BG/aCD40. Therefore, our data identifies a previously unappreciated role for Dectin-1 signaling in unleashing the capacity of aCD40 to invoke productive immunosurveillance.

Dectin-1 signaling can mediate diverse cellular responses, depending on ligation by soluble or particulate BGs, duration of activation, and integration of additional signaling pathways (*27*). In some contexts, chronic Dectin-1 signaling has been implicated in promoting tumorigenesis and T cell evasion (*50*). In contrast, we found that acute activation of Dectin-1 in combination with aCD40 invoked robust antitumor immunity. Several factors may contribute to this, including the use of a soluble BG and the acute nature of Dectin-1 activation in our study. In addition, prior work showed that IFN-γ can sensitize macrophages to Dectin-1–mediated signaling through Spleen tyrosine kinase (Syk) (*51*). Consistent with this, we found IFN-γ to enforce the antitumor activity of BG. This finding suggests that integration of intracellular signaling responses to cytokine receptor and PRR activation can drive context-dependent cellular fates. To this end, our findings show that IFN-γ and BG targeted multiple myeloid cell subsets within the TME. However, the precise roles of distinct myeloid cell subsets remain unclear, including the relative contribution of combinatory cytokine and PRR activation to their cellular fate. Future studies will be needed to elucidate molecular mechanisms by which cytokines modulate cellular outcomes to PRR activation in distinct immune cell subsets.

Our results highlight a key role for noncytotoxic functions of T cells in the antitumor response. Antitumor activity was independent of classical T cell cytotoxicity pathways, because responses were maintained against tumor cells lacking MHC expression and

IFN-γ signaling and in transgenic mouse models deficient in perforin. Loss of tumor MHC expression or sensitivity to IFN-γ are common resistance mechanisms to ICB (*52*), suggesting that combined myeloid activation may be a strategy to overcome immune resistance associated with ICB failure. Moreover, we found that ICB did not augment antitumor immunity induced by combination myeloid-activating therapy, showing that effective myeloid engagement can circumvent the need for blocking immune checkpoint molecules expressed by T cells. Thus, productive cancer immunosurveillance does not necessarily require canonical T cell cytotoxicity pathways or inhibition of T cell immune checkpoints.

Our data suggest that CD40 activation and BG therapy converge at the level of monocytes and TAMs, which may act as antitumor effector cells. TAMs can exert multiple and redundant tumor cytotoxic functions, including production of reactive oxygen species (ROS), nitric oxide (NO), and cytokines and phagocytosis of tumor cells (*53*). In addition, immunostimulatory TAMs can act as antigen-presenting cells (APCs) (*47*), potentially supporting feedforward antitumor immune circuits consisting of tumor-specific T cells and APCs. Hence, a limitation of our study is that our findings provide only partial insight into the specific functional contributions of tumoricidal and antigen-presenting TAM pathways in the setting of BG/aCD40. Future studies aimed at defining the impact and role of discrete monocyte/TAM cytotoxicity pathways on tumor cells may inform promising cancer therapies. In summary, these findings define a previously undescribed immunotherapy paradigm via coactivation of complementary myeloid signaling pathways. A clinical trial (NCT05484011) studying the combination of BG and aCD40 for the treatment of patients with PDA is underway.

MATERIALS AND METHODS

Study design

The goal of this study was to demonstrate the antitumor potential and mechanism of action of combinatory myeloid pathway activation for the treatment of ICB-resistant solid tumors. To test this, we combined an anti-CD40 monoclonal antibody with agonist activity (FGK45) with a soluble BG agonist of the CLR Dectin-1 in ICB-resistant mouse models of pancreatic ductal adenocarcinoma (PDA). To define the cellular and molecular mechanisms underlying the antitumor activity of CD40 and Dectin-1 coactivation, we integrated pharmacologic depletion of immune cell subsets, transgenic mouse models (*Batf3*^{ko}, *Clec7a*^{ko}, and *Prf1*^{ko}), CRISPR-Cas9 engineering of tumor cells (*B2m*^{ko} and *Ifngr1*^{ko}) and orthogonal multi-omics (RNA-seq, scRNA-seq, mass cytometry, and multiplex IHC). Experiments in this study were conducted two or three times unless otherwise specified in the figure legends. In vivo studies were conducted using mice block-randomized to treatment groups in an unblinded manner. No outliers were excluded.

Mice

Eight- to 10-week-old male and female C57BL/6 (stock no. 000664), B6.129S(C)-*Batf3*^{tm1Kmm}/J (stock 013755), C57BL/6-*Prf1*^{tm1Sdz}/J (stock 002407), and B6.129S6-*Clec7a*^{tm1Gdb}/J (stock 012337) mice were ordered from the Jackson Laboratory or bred in house. Mice were housed under pathogen-free conditions in a barrier facility, and animal protocols were reviewed and approved by the Institute of Animal Care and Use Committee at the University of Pennsylvania (protocol number 803605).

Cell lines

Polyclonal PDA.7940B, PDA.69 tumor cells derived from *LSL-Kras*$^{G12D/+}$*;LSL-Trp53*$^{R172H/+}$*;Pdx-1-Cre* mice and clonal PDA.8572.E12 tumor cells derived from KPC mice expressing the yellow fluorescent protein (YFP)–lineage tag were acquired as previously described (*54*) and used in subcutaneous and orthotopic tumor models. Cell culture was conducted using Dulbecco's modified Eagle's medium (DMEM; Corning) supplemented with 10% fetal bovine serum (FBS; VWR), 1% L-glutamine (Thermo Fisher Scientific), and gentamicin (83 μg/ml; Thermo Fisher Scientific) at 37°C and 5% CO_2. All cell lines used routinely tested negative for mycoplasma contamination.

Generation of CRISPR-edited tumor cell lines

PDA.8572.E12 tumor cells were transiently transfected with pX459-Cas9-sgRNA (single guide RNA) targeting *B2m* or *Ifngr1* with Lipofectamine 2000 reagent (Thermo Fisher Scientific). pSpCas9(BB)-2A-Puro (PX459) V2.0 was a gift from F. Zhang (Addgene plasmid no. 62988; http://n2t.net/addgene:62988; RRID:Addgene_62988) (*55*). Transfected tumor cells were selected by applying puromycin (Clontech)–containing medium for 48 hours. Validation of target knockout was conducted on clones generated by limiting dilution. Tumor cells were treated with or without murine IFN-γ (100 ng/ml; PeproTech) for 24 hours, and H-2kb/H-2kd and PD-L1 were assessed by flow cytometry. Knockout of IFNgR1 was also confirmed using flow cytometry. CRISPR sgRNA sequences included *B2m* sgRNA_1 (5′-CTCAAATTCAAGTATACTCA) and *Ifngr1* sgRNA_1 (5′-GGTATTCCCAGCATACGACA).

Tumor models

For subcutaneous tumor models, PDA.7940B cells (5×10^5 or 1×10^6), PDA.69 cells (5×10^5 or 1×10^6), and PDA.8572.E12 (1×10^6) cells were injected subcutaneously into the flanks of mice. For orthotopic tumor models, mice were anesthetized using continuous isoflurane. Once analgesia was administered, depth of anesthesia was evaluated, and sterilization of the abdomen was performed. A laparotomy was made over the left upper quadrant of the abdomen. The spleen and pancreas were exteriorized onto a sterile field, and PDA.7940B cells (5×10^5) were injected into the tail of the pancreas using a 30-gauge needle (Covidien). Observation of a liquid bleb at the site of injection with minimal fluid leakage was used to confirm appropriate injection. The spleen and pancreas were then returned to the peritoneal cavity. The peritoneum was closed with absorbable suture (Ethicon PDS II), and the skin was closed with surgical staples (AutoClip). For secondary tumor challenge, mice that showed tumor eradication after treatment and remained tumor-free for >100 days were rechallenged with 1×10^6 tumor cells injected subcutaneously.

Pancreatectomy model

For pancreatectomy/splenectomy models, an orthotopic tumor was initiated with PDA.7940B cells (1×10^5) and allowed to engraft for 10 days before surgery or initiation of neoadjuvant therapy. In the case of neoadjuvant therapy, surgery was conducted 10 to 14 days after treatment onset. For surgery, mice were anesthetized with continuous isoflurane. Analgesia was administered; depth of anesthesia

was evaluated, and the abdomen was sterilized. A left upper quadrant laparotomy was created, and the distal pancreas and spleen were resected using electrocautery (Gemini). Hemostatic control was maintained. The peritoneum was closed with absorbable suture (Ethicon PDS II), and the skin was closed using surgical staples (AutoClip). In mice treated with neoadjuvant BG/aCD40, before resection of the spleen and pancreas, splenic vessels were ligated using ligation clips (Horizon) to prevent hemorrhage in the setting of treatment-related splenomegaly. Necropsy was performed at time of death, and mice were confirmed to have progressive cancer (presence of recurrent pancreatic tumor and metastases to liver, lung, peritoneum, or lymph node) were included in the survival analysis.

Animal treatment protocol

Sex-matched 8- to 10-week-old mice were block-randomized in an unblinded manner. Sample sizes were estimated on the basis of pilot studies to provide adequate numbers of mice in each group for statistical analysis. Mice were monitored three times per week and euthanized on the basis of defined criteria including tumor volume >1000 mm^3, loss of >20% body weight, lethargy, or other signs of distress. For subcutaneous studies, mice (<1%) in which tumors did not establish or were euthanized because of distress despite no significant tumor outgrowth were excluded. For antibody treatments of mice, the abdomen was sterilized, and antibodies diluted in 100 μl of phosphate-buffered saline (PBS) were administered by intraperitoneal injection using a 30-guage needle. Anti-CD40 (clone FGK45; catalog no. BE0016-2; RRID: AB_1107647; 0.1 mg) was administered on day 0. Mice (~5%) that did not show depletion of $CD19^+$ B cells at 24 hours after treatment with anti-CD40 were excluded as previously described (*30*). For T cell depletion, anti-CD4 (clone GK1.5; catalog no. BE0003-1; RRID: AB_1107636; 0.2 mg) and anti-CD8 (clone 2.43; catalog no. BE0061; RRID: AB_1125541; 0.2 mg) were given on days −3, 0, 4, 7, and 11 unless otherwise specified. Anti-Ly6C (clone MONTS1; catalog no. BE0203; RRID: AB_2687696; 0.5 mg) was delivered on days −1, 0, 1, 5, and 9. Anti-CD20 (clone MB20-11; catalog no. BE0356; RRID: AB_2894775; 0.2 mg) was given on day −1. Anti-Ly6G (clone 1A8; catalog no. BP0075-1) was administered on day −1 (0.5 mg) and days 0, 1, 5, and 9 (0.2 mg). Anti–PD-1 (clone RMP1-14; catalog no. BE0146; RRID: AB_10949053; 0.2 mg) was given on days 0, 4, and 7 (neoadjuvant); days 7, 11, and 14 (adjuvant); or days −3, 0, 3, 6, 9, 12, 15, 18, and 21. Anti–CTLA-4 (clone 9H10; catalog no. BE0131; RRID: AB_10950184; 0.2 mg) was given on days −3, 0, 3, and 6. All antibodies were purchased from Bio X Cell. Gemcitabine (120 mg/kg) and nab-paclitaxel (120 mg/kg) were suspended in PBS and administered by intraperitoneal injection on day −2. Imprime PGG (odetiglucan) is a clinical-grade soluble, β-1,3/1,6 glucan derived from *Saccharomyces cerevisiae* (*28*). Imprime labeled with 5-(4,6-dichlorotriazinyl) aminofluorescein (5-DTAF), a reactive dye with absorption/emission maxima of 492/516, was used for binding studies. BG and BG-DTAF (1.2 mg; HiberCell Inc.) were systemically delivered via tail-vein or intraperitoneal injection in 100 μl of PBS using a 30-guage needle on day 0. Clodronate-encapsulated liposomes (Liposoma) were administered by intraperitoneal injection, as per the manufacturer's instructions, on days −2, 0, 2, 5, and 9. GW2580 (160 mg/kg; Selleckchem) was diluted in 0.5% hydroxypropylmethylcellulose and 0.1% Tween-80 and administered by oral gavage on days −2, −1, 0, 1, 2, 5, 6, 7, 8, and 9. Pam3CSK4 (0.2 mg; InvivoGen), lipopolysaccharide (50 μg; InvivoGen), CpG (50 μg; InvivoGen), R848 (50 μg; InvivoGen), DMXAA (0.5 mg; InvivoGen), and MDP (0.3 mg; InvivoGen) were diluted in sterile water and administered by intraperitoneal injection on day 0. For intratumoral treatment, mouse recombinant IFN-γ (3 μg; PeproTech) was suspend in 50 μl of PBS and administered intratumorally.

Cytokine and AST/ALT analysis

Blood was obtained by retro-orbital collection and centrifuged at 13,000 rpm for 20 min. Serum was collected and stored at −80°C until use. Aspartate transaminase (AST) and alanine transaminase (ALT) levels were acquired by IDEXX BioAnalytics. Cytokines were measured using Luminex assay.

Flow cytometry

Flow cytometry staining and acquisition were conducted as previously described (*54*, *56*). Briefly, peripheral blood was collected by tail vein bleed, incubated in ACK lysing buffer (Life Technologies) for 5 min, and washed with PBS. Single cells were isolated from spleen and lymph node by mechanical dissociation followed by filtering through a 70-μm nylon strainer (Corning). Tumors were minced with microdissecting scissors at 4°C in DMEM containing collagenase (1 mg/ml; Sigma-Aldrich) and deoxyribonuclease (DNase; 150 U/ml; Sigma) and incubated at 37°C for 45 min with intermittent agitation. Tissues were filtered through a 70-μm nylon strainer (Corning). Cells were then incubated in ACK lysing buffer (Life Technologies) for 5 min, washed with DMEM, counted using a TC20 automated cell counter (Bio-Rad), and stained using Aqua dead cell stain kit (Life Technologies) for 20 min at room temperature. After washing, cells were incubated with a master mix of primary conjugated antibodies for surface staining for 30 min at 4°C. For intracellular staining, cells were permeabilized using Fixation/Permeabilization Buffer (eBioscience) followed by incubation with primary conjugated antibodies. The antibodies used are described in table S3. Data acquisition was performed on a FACSCanto II (BD Biosciences). Analysis of flow cytometric data was performed using FlowJo version 10.2 (BD).

Mass cytometry

For mass cytometry processing, orthotopic tumors were processed in the same manner as for flow cytometry and then filtered through a 70-μm nylon strainer (Corning), washed with metal-free FACS buffer (PBS, 0.2 mM EDTA, and 2% FBS), and incubated in ACK lysing buffer (Life Technologies) for 5 min. After washing in FACS buffer, cells were incubated in 1 mM 198PT monoisotopic cisplatin (Fluidigm), fixed in Cytofix fixation buffer (BD), and cryopreserved until staining. Thawed cells were counted and washed, and 2×10^6 cells or fewer per sample were barcoded by incubation with palladium metal tags as per the manufacturer's instructions (Fluidigm). Pooled cells were then incubated with permeabilization working solution (eBioscience) with 2% mouse serum and mouse anti-CD16/32 and stained with a lymphoid or myeloid-focused antibody master mix (tables S4 and S5) for 30 min at room temperature. Cells were washed and fixed in 2.4% formaldehyde with iridium nucleic acid intercalator (125 nM; Fluidigm) overnight at 4°C. Cells were cryopreserved and stored at −80°C until acquisition on a Helios mass cytometer (Fluidigm). Acquisition was performed with cells resuspended at a concentration of 1×10^6 cells/ml in cell acquisition

solution with 5% EQ beads (Fluidigm). Bead normalization and debarcoding of flow cytometry standard (FCS) files was performed using Helios software (Fluidigm). Events were gated to remove doublets and dead cells and for positive or negative selection of markers of interest (CD45, CD3, and $CD3^{neg}B220^{neg}$) using FlowJo version 10.2 (BD). TSNE analysis, phenograph (*57*), and FlowSOM (*58*) clustering were performed using the cytofkit2 and visualized with ggplot2 packages in R. Density plots were generated using the stat_density_2d function and UMAPs using the umap package (V0.2.10.0) R package. Heatmaps were made using the Pheatmap package (v1.0.12) in R.

Microscopic analysis

Mouse tissues were fixed in 10% formalin for 48 hours at room temperature, washed twice in PBS, and stored in 70% ethanol at 4°C. Tissues were processed and embedded to generate formalin-fixed paraffin-embedded (FFPE) blocks. Specimens were sectioned at 5 μm onto Superfrost Plus microscope slides (VWR International, catalog 48311-703). Automated IHC and RNA in situ hybridization were performed using a Ventana Discovery Ultra automated slide staining system (Roche). The following primary antibodies were used against mouse antigens: CD3 (Abcam, Polyclonal; catalog no. ab5690; RRID: AB_305055), Ki67 (Cell Signaling Technology; Clone D3B5; catalog no. 12202; RRID: AB_2620142), F4/80 (Cell Signaling Technology; Clone D2S9R; catalog no. 70076; RRID: AB_2799771), pSTAT1 (Cell Signaling Technology, Clone 58D6; catalog no. 9167; RRID: AB_561284), CD206 (Abcam; Clone EPR25215; catalog no. Ab300621; RRID: AB_2935881), and CK19 (Abcam; Clone EPNCIR127B; catalog no. ab133496; RRID: AB_11155282). RNA in situ hybridization reagents were obtained from ACDBio. Staining was performed as previously described (*59*). Briefly, slides were baked and deparaffinized, followed by heat-induced epitope retrieval using Cell Conditioning Solution (Roche), sequential incubation with discovery inhibitor (Roche), and S block (Roche). Slides were then stained with primary antibody, linking antibody, and then chromogen substrate. Stained slides were air-dried at room temperature.

IHC image analysis

Whole slide images were obtained using an Aperio C2 scanner (Leica) and analyzed using algorithms developed with Visiopharm Integrator System software (version 2020.01). Cells were detected and classified on the basis of colorimetric characteristics within regions of interest (ROIs) using custom algorithms. ROIs were manually delineated around regions of tumor (intratumoral ROI, defined by CK19) or the tumor border (border ROI, defined from the edge of CK19-positive regions to the tumor edge). Regions containing adipose tissue, necrotic lesions, and artifactual staining were excluded from analysis. Immune infiltrates were quantified within the ROI. Cell numbers were normalized to ROI area and expressed as densities (cells per mm^2) or percentage of ROI (F4/80 and CK19). $CD3^+$ cell density plots were generated using Visiopharm.

RNA isolation and sequencing

Total RNA was extracted from 5-μm serial sections obtained from FFPE tissues using the RNeasy FFPE kit (QIAGEN). Preparation of a standard RNA library was performed by the Wistar Institute Genomics Facility. Briefly, 3′ mRNA-seq libraries were generated from 100 ng of DNase I–treated total RNA using the QuantSeq FWD Library Preparation Kit (Hexogen) according to the manufacturer′s directions. Overall library size was determined using the Agilent TapeStation and the DNA 5000 ScreenTape (Agilent). Libraries were quantitated using real-time polymerase chain reaction (PCR; Kapa Biosystems). Libraries were pooled, and single-read, 100–base pair next-generation sequencing was performed on a NextSeq 2000 (Illumina).

Analysis of RNA-seq data

Reads were mapped to the GRCm38/mm10 genome using the BaseSpace Suite (Illumina). Gene expression was normalized, and differential gene expression was calculated across groups using DESeq2 (v1.32.0) (*60*). A gene was considered differentially expressed between two groups with an adjusted P value of <0.01 and $\log_2$ fold change >1.2 or <−1.2. Principal components analysis (PCA) was performed on all detected genes using the regular log transformation from DESeq2. Data were visualized using volcano plots from DESeq2 and heatmaps from the Pheatmap R package (v1.0.12). Gene set enrichment analysis was conducted using the GSEABase (v1.54.0) R package. Radar plots were generated using the fmsb package (v0.7.5) in R.

Single-cell sequencing

Two samples (consisting of two or three pooled tumors) per treatment condition were processed for scRNA-seq. After tissue digest of orthotopic tumors as described above, next-generation sequencing libraries were prepared using the 10x Genomics Chromium Single Cell 3′ Reagent kit v3.1 per the manufacturer′s instructions. Libraries were uniquely indexed using the Chromium dual Index Kit, pooled, and sequenced on an Illumina NovaSeq 6000 sequencer in a paired-end, dual-indexing run. Sequencing for each library targeted 20,000 mean reads per cell. Data were then processed using the Cell Ranger pipeline (10x Genomics, v.6.1.2) for demultiplexing and alignment of sequencing reads to the mm10 transcriptome and creation of feature-barcode matrices.

Single-cell sequencing analysis

For analysis of previously published scRNA-seq datasets (*16*, *23*–*25*, *31*) counts, gene information, and barcode matrix output were downloaded from the NIH Gene Expression Omnibus database [www.ncbi.nlm.nih.gov/geo/; accession numbers GSE155698 (human PDA), GSE163120 (human GBM), GSE164690 (human HNSCC), and GSE125588 (spontaneous mouse models of PDA)] and www.cancerdiversity.asia/scCRLM/ (human CRC). Analysis was performed using Seurat (version 4.04; https://satijalab.org/seurat/) (*61*) and R (version 4.1.1) (*62*). For quality control, data were filtered to include cells with a minimum of 200 genes, and genes that were present in greater than three cells were included. Cells that contained reads for more than 2500 or fewer than 200 genes were excluded, as were cells that contained more than 30% of reads aligned to mitochondrial genes. Data were normalized using the NormalizeData function with the LogNormalize method and scale factor of 10^4. Highly variable genes (n = 2000) were identified with the "vst" selection method, and genes were scaled and centered to a mean of 0 using the ScaleData function. The RunPCA function was applied using previously identified genes for linear dimensionality reduction. Batch correction was performed using the R package Harmony (version 1.0) (*63*). The FindNeighbors and FindClusters functions were implemented to

identify cell clusters using a resolution of 0.5 (all cells, lymphoid cells) or 0.4 (TAM and monocytes). Nonlinear dimensionality reduction was performed using the RunUmap feature to visualize clusters in a two-dimensional space. Cluster markers were identified using the FindAllMarkers function, testing for DEGs between cells in a single cluster as compared with all other clusters. Clusters were defined by manual review of cluster-specific DEGs and the MyGeneSet tool (ImmGen). DEG analysis was conducted using FindMarkers. A gene was considered differentially expressed between two groups with an adjusted P value of <0.05 and $\log_2$ fold change >0.8 or <−0.8. Gene signatures were generated using AddModuleScore and visualized by feature plot using FeaturePlot_scCustom in the scCustomize R package. For heatmaps of DEGs, the average of each gene was calculated using AverageExpression, scaled, and visualized using DoHeatmap. Pseudotime analysis was conducted using Monocle3.

Statistical analysis

Student's t tests and Mann-Whitney U tests were used for comparison of unpaired variables, using a two-sided alpha of 0.05. Where appropriate, multiple comparison testing was performed using one- or two-way analysis of variance (ANOVA) with Tukey's test with a false discovery rate <0.05. Survival analysis was conducted using Kaplan-Meier methodology, and log-rank (Mantle Cox) was used to compare survival between groups. Spearman correlation coefficients were calculated to quantify correlations between features. Statistical analysis was conducted using Prism (GraphPad Software, version 9.2.0) and R (version 4.1.1) (*62*).

Supplementary Materials

This PDF file includes:
Figs. S1 to S10
Tables S1 to S5

Other Supplementary Material for this manuscript includes the following:
Data file S1
MDAR Reproducibility Checklist

REFERENCES AND NOTES

1. A. D. Waldman, J. M. Fritz, M. J. Lenardo, A guide to cancer immunotherapy: From T cell basic science to clinical practice. *Nat. Rev. Immunol.* **20**, 651–668 (2020).
2. D. J. Renouf, J. M. Loree, J. J. Knox, J. T. Topham, P. Kavan, D. Jonker, S. Welch, F. Couture, F. Lemay, M. Tehfe, M. Harb, N. Aucoin, Y.-J. Ko, P. A. Tang, R. Ramjeesingh, B. M. Meyers, C. A. Kim, P. du, S. Jia, D. F. Schaeffer, S. Gill, D. Tu, C. J. O'Callaghan, The CCTG PA.7 phase II trial of gemcitabine and nab-paclitaxel with or without durvalumab and tremelimumab as initial therapy in metastatic pancreatic ductal adenocarcinoma. *Nat. Commun.* **13**, 5020 (2022).
3. D. A. Reardon, A. A. Brandes, A. Omuro, P. Mulholland, M. Lim, A. Wick, J. Baehring, M. S. Ahluwalia, P. Roth, O. Bähr, S. Phuphanich, J. M. Sepulveda, P. de Souza, S. Sahebjam, M. Carleton, K. Tatsuoka, C. Taitt, R. Zwirtes, J. Sampson, M. Weller, Effect of nivolumab vs bevacizumab in patients with recurrent glioblastoma: The checkmate 143 phase 3 randomized clinical trial. *JAMA Oncol.* **6**, 1003–1010 (2020).
4. C. Eng, T. W. Kim, J. Bendell, G. Argilés, N. C. Tebbutt, M. di Bartolomeo, A. Falcone, M. Fakih, M. Kozloff, N. H. Segal, A. Sobrero, Y. Yan, I. Chang, A. Uyei, L. Roberts, F. Ciardiello, J.-B. Ahn, J. Asselah, S. Badarinath, S. Baijal, S. Begbie, S. Berry, J.-L. Canon, R.-G. Carbone, A. Cervantes, Y.-J. Cha, K. Chang, A. Chaudhry, E. Chmielowska, S.-H. Cho, D. Chu, F. Couture, J. Cultrera, D. Cunningham, E. van Cutsem, P. J. Cuyle, J. Davies, S. Dowden, M. Dvorkin, V. Ganju, R. V. Garcia, R. Kerr, T.-Y. Kim, K. King, J. Kortmansky, M. Kozloff, K. O. Lam, J. Lee, A.-S. Lee, B. Lesperance, G. Luppi, B. Ma, E. Maiello, R. Mandanas, J. Marshall, G. Marx, S. Mullamitha, M. Nechaeva, J.-O. Park, N. Pavlakis, C. G. Ponce, P. Potemski, S. Raouf, J. Reeves, N. Segal, S. Siena, A. Smolin, J. O. Streb, A. Strickland, E. Szutowicz-Zielinska, J. M. Tabernero, B. Tan, J. S. Valera, M. van den Eynde, P. Vergauwe, M. Vickers, M. Womack, M. Wroblewska, R. Young, Atezolizumab with or without cobimetinib versus regorafenib in previously treated metastatic colorectal cancer (IMblaze370): A multicentre, open-label, phase 3, randomised, controlled trial. *Lancet Oncol.* **20**, 849–861 (2019).
5. D. S. Chen, I. Mellman, Oncology meets immunology: The cancer-immunity cycle. *Immunity* **39**, 1–10 (2013).
6. P. C. Tumeh, C. L. Harview, J. H. Yearley, I. P. Shintaku, E. J. M. Taylor, L. Robert, B. Chmielowski, M. Spasic, G. Henry, V. Ciobanu, A. N. West, M. Carmona, C. Kivork, E. Seja, G. Cherry, A. J. Gutierrez, T. R. Grogan, C. Mateus, G. Tomasic, J. A. Glaspy, R. O. Emerson, H. Robins, R. H. Pierce, D. A. Elashoff, C. Robert, A. Ribas, PD-1 blockade induces responses by inhibiting adaptive immune resistance. *Nature* **515**, 568–571 (2014).
7. D. S. Chen, I. Mellman, Elements of cancer immunity and the cancer-immune set point. *Nature* **541**, 321–330 (2017).
8. S. T. Barry, D. I. Gabrilovich, O. J. Sansom, A. D. Campbell, J. P. Morton, Therapeutic targeting of tumour myeloid cells. *Nat. Rev. Cancer* **23**, 216–237 (2023).
9. M. Najafi, N. Hashemi Goradel, B. Farhood, E. Salehi, M. S. Nashtaei, N. Khanlarkhani, Z. Khezri, J. Majidpoor, M. Abouzaripour, M. Habibi, I. R. Kashani, K. Mortezaee, Macrophage polarity in cancer: A review. *J. Cell. Biochem.* **120**, 2756–2765 (2019).
10. M. D. Park, A. Silvin, F. Ginhoux, M. Merad, Macrophages in health and disease. *Cell* **185**, 4259–4279 (2022).
11. M. M. Wattenberg, G. L. Beatty, Overcoming immunotherapeutic resistance by targeting the cancer inflammation cycle. *Semin. Cancer Biol.* **65**, 38–50 (2020).
12. M. Chaib, S. C. Chauhan, L. Makowski, Friend or foe? recent strategies to target myeloid cells in cancer. *Front. Cell Dev. Biol.* **8**, 351 (2020).
13. D. E. Sanford, B. A. Belt, R. Z. Panni, A. Mayer, A. D. Deshpande, D. Carpenter, J. B. Mitchem, S. M. Plambeck-Suess, L. A. Worley, B. D. Goetz, A. Wang-Gillam, T. J. Eberlein, D. G. Denardo, S. P. Goedegebuure, D. C. Linehan, Inflammatory monocyte mobilization decreases patient survival in pancreatic cancer: A role for targeting the CCL2/CCR2 axis. *Clin. Cancer Res.* **19**, 3404–3415 (2013).
14. C. W. Steele, S. A. Karim, J. D. G. Leach, P. Bailey, R. Upstill-Goddard, L. Rishi, M. Foth, S. Bryson, K. McDaid, Z. Wilson, C. Eberlein, J. B. Candido, M. Clarke, C. Nixon, J. Connelly, N. Jamieson, C. R. Carter, F. Balkwill, D. K. Chang, T. R. J. Evans, D. Strathdee, A. V. Biankin, R. J. B. Nibbs, S. T. Barry, O. J. Sansom, J. P. Morton, CXCR2 inhibition profoundly suppresses metastases and augments immunotherapy in pancreatic ductal adenocarcinoma. *Cancer Cell* **29**, 832–845 (2016).
15. M. H. Sherman, G. L. Beatty, Tumor microenvironment in pancreatic cancer pathogenesis and therapeutic resistance. *Annu. Rev. Pathol.* **18**, 123–148 (2023).
16. N. G. Steele, E. S. Carpenter, S. B. Kemp, V. Sirihorachai, S. The, L. Delrosario, J. Lazarus, E.-A. D. Amir, V. Gunchick, C. Espinoza, S. Bell, L. Harris, F. Lima, V. Irizarry-Negron, D. Paglia, J. Macchia, A. K. Y. Chu, H. Schofield, E.-J. Wamsteker, R. Kwon, A. Schulman, A. Prabhu, R. Law, A. Sondhi, J. Yu, A. Patel, K. Donahue, H. Nathan, C. Cho, M. A. Anderson, V. Sahai, C. A. Lyssiotis, W. Zou, B. L. Allen, A. Rao, H. C. Crawford, F. Bednar, T. L. Frankel, M. P. di Magliano, Multimodal mapping of the tumor and peripheral blood immune landscape in human pancreatic cancer. *Nature. Nat Cancer* **1**, 1097–1112 (2020).
17. G. L. Beatty, Y. Li, K. B. Long, Cancer immunotherapy: Activating innate and adaptive immunity through CD40 agonists. *Expert Rev. Anticancer Ther.* **17**, 175–186 (2017).
18. R. H. Vonderheide, The immune revolution: A case for priming, not checkpoint. *Cancer Cell* **33**, 563–569 (2018).
19. M. H. O'Hara, E. M. O'Reilly, G. Varadhachary, R. A. Wolff, Z. A. Wainberg, A. H. Ko, G. Fisher, O. Rahma, J. P. Lyman, C. R. Cabanski, R. Mick, P. F. Gherardini, L. J. Kitch, J. Xu, T. Samuel, J. Karakunnel, J. Fairchild, S. Bucktrout, T. M. LaVallee, C. Selinsky, J. E. Till, E. L. Carpenter, C. Alanio, K. T. Byrne, R. O. Chen, O. C. Trifan, U. Dugan, C. Horak, V. M. Hubbard-Lucey, E. J. Wherry, R. Ibrahim, R. H. Vonderheide, CD40 agonistic monoclonal antibody APX005M (sotigalimab) and chemotherapy, with or without nivolumab, for the treatment of metastatic pancreatic adenocarcinoma: An open-label, multicentre, phase 1b study. *Lancet Oncol.* **22**, 118–131 (2021).
20. L. J. Padrón, D. M. Maurer, M. H. O'Hara, E. M. O'Reilly, R. A. Wolff, Z. A. Wainberg, A. H. Ko, G. Fisher, O. Rahma, J. P. Lyman, C. R. Cabanski, J. X. Yu, S. M. Pfeiffer, M. Spasic, J. Xu, P. F. Gherardini, J. Karakunnel, R. Mick, C. Alanio, K. T. Byrne, T. J. Hollmann, J. S. Moore, D. D. Jones, M. Tognetti, R. O. Chen, X. Yang, L. Salvador, E. J. Wherry, U. Dugan, J. O'Donnell-Tormey, L. H. Butterfield, V. M. Hubbard-Lucey, R. Ibrahim, J. Fairchild, S. Bucktrout, T. M. La Vallee, R. H. Vonderheide, Sotigalimab and/or nivolumab with chemotherapy in first-line metastatic pancreatic cancer: Clinical and immunologic analyses from the randomized phase 2 PRINCE trial. *Nat. Med.* **28**, 1167–1177 (2022).
21. G. L. Beatty, D. A. Torigian, E. G. Chiorean, B. Saboury, A. Brothers, A. Alavi, A. B. Troxel, W. Sun, U. R. Teitelbaum, R. H. Vonderheide, P. J. O'Dwyer, A phase I study of an agonist CD40 monoclonal antibody (CP-870,893) in combination with gemcitabine in patients with advanced pancreatic ductal adenocarcinoma. *Clin. Cancer Res.* **19**, 6286–6295 (2013).
22. O. Takeuchi, S. Akira, Pattern recognition receptors and inflammation. *Cell* **140**, 805–820 (2010).

23. A. R. Pombo Antunes, I. Scheyltjens, F. Lodi, J. Messiaen, A. Antoranz, J. Duerinck, D. Kancheva, L. Martens, K. de Vlaminck, H. van Hove, S. S. Kjølner Hansen, F. M. Bosisio, K. van der Borght, S. de Vleeschouwer, R. Sciot, L. Bouwens, M. Verfaillie, N. Vandamme, R. E. Vandenbroucke, O. de Wever, Y. Saeys, M. Guilliams, C. Gysemans, B. Neyns, F. de Smet, D. Lambrechts, J. A. van Ginderachter, K. Movahedi, Single-cell profiling of myeloid cells in glioblastoma across species and disease stage reveals macrophage competition and specialization. *Nat. Neurosci.* **24**, 595–610 (2021).
24. Y. Wu, S. Yang, J. Ma, Z. Chen, G. Song, D. Rao, Y. Cheng, S. Huang, Y. Liu, S. Jiang, J. Liu, X. Huang, X. Wang, S. Qiu, J. Xu, R. Xi, F. Bai, J. Zhou, J. Fan, X. Zhang, Q. Gao, Spatiotemporal immune landscape of colorectal cancer liver metastasis at single-cell level. *Cancer Discov.* **12**, 134–153 (2021).
25. C. H. L. Kürten, A. Kulkarni, A. R. Cillo, P. M. Santos, A. K. Roble, S. Onkar, C. Reeder, S. Lang, X. Chen, U. Duvvuri, S. Kim, A. Liu, T. Tabib, R. Lafyatis, J. Feng, S.-J. Gao, T. C. Bruno, D. A. A. Vignali, X. Lu, R. Bao, L. Vujanovic, R. L. Ferris, Investigating immune and non-immune cell interactions in head and neck tumors by single-cell RNA sequencing. *Nat. Commun.* **12**, 7338 (2021).
26. J. W. Lee, C. A. Komar, F. Bengsch, K. Graham, G. L. Beatty, Genetically engineered mouse models of pancreatic cancer: The KPC model (LSL-Kras(G12D/+) ;LSL-Trp53(R172H/+) ;Pdx-1-Cre), its variants, and their application in immuno-oncology drug discovery. *Curr. Protoc. Pharmacol.* **73**, 14 39 1–14 39 20 (2016).
27. T. B. H. Geijtenbeek, S. I. Gringhuis, Signalling through C-type lectin receptors: Shaping immune responses. *Nat. Rev. Immunol.* **9**, 465–479 (2009).
28. N. Bose, N. R. Ottoson, X. Qiu, B. Harrison, J. R. Lowe, M. T. Uhlik, B. T. Rathmann, T. O. Kangas, L. R. Jordan, K. E. Ertelt, A. B. Jonas, R. M. Walsh, A. S. H. Chan, R. B. Fulton, S. M. Leonardo, K. A. Fraser, K. B. Gorden, M. A. Matson, J. R. Graff, R. D. Huhn, Immune pharmacodynamic responses of the novel cancer immunotherapeutic imprime PGG in healthy volunteers. *J. Immunol.* **202**, 2945–2956 (2019).
29. M. Thomas, P. Sadjadian, J. Kollmeier, J. Lowe, P. Mattson, J. R. Trout, M. Gargano, M. L. Patchen, R. Walsh, M. Beliveau, J. F. Marier, N. Bose, K. Gorden, F. Schneller III, A randomized, open-label, multicenter, phase II study evaluating the efficacy and safety of BTH1677 (1,3-1,6 beta glucan; Imprime PGG) in combination with cetuximab and chemotherapy in patients with advanced non-small cell lung cancer. *Invest. New Drugs* **35**, 345–358 (2017).
30. M. L. Stone, J. Lee, V. M. Herrera, K. Graham, J. W. Lee, A. Huffman, H. Coho, E. Tooker, M. I. Myers, M. Giannone, Y. Li, T. H. Buckingham, K. B. Long, G. L. Beatty, TNF blockade uncouples toxicity from antitumor efficacy induced with CD40 chemoimmunotherapy. *JCI Insight* **6**, e146314 (2021).
31. A. N. Hosein, H. Huang, Z. Wang, K. Parmar, W. Du, J. Huang, A. Maitra, E. Olson, U. Verma, R. A. Brekken, Cellular heterogeneity during mouse pancreatic ductal adenocarcinoma progression at single-cell resolution. *JCI Insight* **5**, e129212 (2019).
32. N.-B. Hao, M.-H. Lü, Y.-H. Fan, Y.-L. Cao, Z.-R. Zhang, S.-M. Yang, Macrophages in tumor microenvironments and the progression of tumors. *Clin. Dev. Immunol.* **2012**, 948098 (2012).
33. D. D. Von Hoff, T. Ervin, F. P. Arena, E. G. Chiorean, J. Infante, M. Moore, T. Seay, S. A. Tjulandin, W. W. Ma, M. N. Saleh, M. Harris, M. Reni, S. Dowden, D. Laheru, N. Bahary, R. K. Ramanathan, J. Tabernero, M. Hidalgo, D. Goldstein, E. Van Cutsem, X. Wei, J. Iglesias, M. F. Renschler, Increased survival in pancreatic cancer with nab-paclitaxel plus gemcitabine. *N. Engl. J. Med.* **369**, 1691–1703 (2013).
34. D. P. S. Sohal, M. Duong, S. A. Ahmad, N. S. Gandhi, M. S. Beg, A. Wang-Gillam, J. L. Wade III, E. G. Chiorean, K. A. Guthrie, A. M. Lowy, P. A. Philip, H. S. Hochster, Efficacy of perioperative chemotherapy for resectable pancreatic adenocarcinoma: A phase 2 randomized clinical trial. *JAMA Oncol.* **7**, 421–427 (2021).
35. T. Conroy, P. Hammel, M. Hebbar, M. Ben Abdelghani, A. C. Wei, J.-L. Raoul, L. Choné, E. Francois, P. Artru, J. J. Biagi, T. Lecomte, E. Assenat, R. Faroux, M. Ychou, J. Volet, A. Sauvanet, G. Breysacher, F. di Fiore, C. Cripps, P. Kavan, P. Texereau, K. Bouhier-Leporrier, F. Khemissa-Akouz, J.-L. Legoux, B. Juzyna, S. Gourgou, C. J. O'Callaghan, C. Jouffroy-Zeller, P. Rat, D. Malka, F. Castan, J.-B. Bachet, FOLFIRINOX or gemcitabine as adjuvant therapy for pancreatic cancer. *N. Engl. J. Med.* **379**, 2395–2406 (2018).
36. A. H. Morrison, M. S. Diamond, C. A. Hay, K. T. Byrne, R. H. Vonderheide, Sufficiency of CD40 activation and immune checkpoint blockade for T cell priming and tumor immunity. *Proc. Natl. Acad. Sci. U.S.A.* **117**, 8022–8031 (2020).
37. K. T. Byrne, R. H. Vonderheide, CD40 stimulation obviates innate sensors and drives T cell immunity in cancer. *Cell Rep.* **15**, 2719–2732 (2016).
38. S. Leibundgut-Landmann, F. Osorio, G. D. Brown, C. Reis e Sousa, Stimulation of dendritic cells via the dectin-1/Syk pathway allows priming of cytotoxic T-cell responses. *Blood* **112**, 4971–4980 (2008).
39. S. Halle, O. Halle, R. Forster, Mechanisms and dynamics of T cell-mediated cytotoxicity in vivo. *Trends Immunol.* **38**, 432–443 (2017).
40. D. Kägi, B. Ledermann, K. Bürki, P. Seiler, B. Odermatt, K. J. Olsen, E. R. Podack, R. M. Zinkernagel, H. Hengartner, Cytotoxicity mediated by T cells and natural killer cells is greatly impaired in perforin-deficient mice. *Nature* **369**, 31–37 (1994).
41. M. D. Pilato, R. Kfuri-Rubens, J. N. Pruessmann, A. J. Ozga, M. Messemaker, B. L. Cadilha, R. Sivakumar, C. Cianciaruso, R. D. Warner, F. Marangoni, E. Carrizosa, S. Lesch, J. Billingsley, D. Perez-Ramos, F. Zavala, E. Rheinbay, A. D. Luster, M. Y. Gerner, S. Kobold, M. J. Pittet, T. R. Mempe, CXCR6 positions cytotoxic T cells to receive critical survival signals in the tumor microenvironment. *Cell* **184**, 4512–4530.e22 (2021).
42. C. Gerlach, E. A. Moseman, S. M. Loughhead, D. Alvarez, A. J. Zwijnenburg, L. Waanders, R. Garg, J. C. de la Torre, U. H. von Andrian, The chemokine receptor CX3CR1 defines three antigen-experienced CD8 T cell subsets with distinct roles in immune surveillance and homeostasis. *Immunity* **45**, 1270–1284 (2016).
43. F. J. Lowery, S. Krishna, R. Yossef, N. B. Parikh, P. D. Chatani, N. Zacharakis, M. R. Parkhurst, N. Levin, S. Sindiri, A. Sachs, K. J. Hitscherich, Z. Yu, N. R. Vale, Y.-C. Lu, Z. Zheng, L. Jia, J. J. Gartner, V. K. Hill, A. R. Copeland, S. K. Nah, R. V. Masi, B. Gasmi, S. Kivitz, B. C. Paria, M. Florentin, S. P. Kim, K.-I. Hanada, Y. F. Li, L. T. Ngo, S. Ray, M. L. Shindorf, S. T. Levi, R. Shepherd, C. Toy, A. Y. Parikh, T. D. Prickett, M. C. Kelly, R. Beyer, S. L. Goff, J. C. Yang, P. F. Robbins, S. A. Rosenberg, Molecular signatures of antitumor neoantigen-reactive T cells from metastatic human cancers. *Science* **375**, 877–884 (2022).
44. L. B. Ivashkiv, IFNγ: Signalling, epigenetics and roles in immunity, metabolism, disease and cancer immunotherapy. *Nat. Rev. Immunol.* **18**, 545–558 (2018).
45. A. M. Gocher, C. J. Workman, D. A. A. Vignali, Interferon-γ: Teammate or opponent in the tumour microenvironment? *Nat. Rev. Immunol.* **22**, 158–172 (2022).
46. M. Revel, C. Sautes-Fridman, W. H. Fridman, L. T. Roumenina, C1q+ macrophages: Passengers or drivers of cancer progression. *Trends Cancer* **8**, 517–526 (2022).
47. Y. Zhu, J. M. Herndon, D. K. Sojka, K.-W. Kim, B. L. Knolhoff, C. Zuo, D. R. Cullinan, J. Luo, A. R. Bearden, K. J. Lavine, W. M. Yokoyama, W. G. Hawkins, R. C. Fields, G. J. Randolph, D. G. DeNardo, Tissue-resident macrophages in pancreatic ductal adenocarcinoma originate from embryonic hematopoiesis and promote tumor progression. *Immunity* **47**, 323–338.e6 (2017).
48. M. Liu, R. S. O'Connor, S. Trefely, K. Graham, N. W. Snyder, G. L. Beatty, Metabolic rewiring of macrophages by CpG potentiates clearance of cancer cells and overcomes tumor-expressed CD47-mediated 'don't-eat-me' signal. *Nat. Immunol.* **20**, 265–275 (2019).
49. T. M. Nywening, B. A. Belt, D. R. Cullinan, R. Z. Panni, B. J. Han, D. E. Sanford, R. C. Jacobs, J. Ye, A. A. Patel, W. E. Gillanders, R. C. Fields, D. G. DeNardo, W. G. Hawkins, P. Goedegebuure, D. C. Linehan, Targeting both tumour-associated $CXCR2^+$ neutrophils and $CCR2^+$ macrophages disrupts myeloid recruitment and improves chemotherapeutic responses in pancreatic ductal adenocarcinoma. *Gut* **67**, 1112–1123 (2018).
50. D. Daley, V. R. Mani, N. Mohan, N. Akkad, A. Ochi, D. W. Heindel, K. B. Lee, C. P. Zambirinis, G. S. D. B. Pandian, S. Savadkar, A. Torres-Hernandez, S. Nayak, D. Wang, M. Hundeyin, B. Diskin, B. Aykut, G. Werba, R. M. Barilla, R. Rodriguez, S. Chang, L. Gardner, L. K. Mahal, B. Ueberheide, G. Miller, Dectin 1 activation on macrophages by galectin 9 promotes pancreatic carcinoma and peritumoral immune tolerance. *Nat. Med.* **23**, 556–567 (2017).
51. D. M. Underhill, E. Rossnagle, C. A. Lowell, R. M. Simmons, Dectin-1 activates Syk tyrosine kinase in a dynamic subset of macrophages for reactive oxygen production. *Blood* **106**, 2543–2550 (2005).
52. A. Kalbasi, A. Ribas, Tumour-intrinsic resistance to immune checkpoint blockade. *Nat. Rev. Immunol.* **20**, 25–39 (2020).
53. K. B. Long, G. L. Beatty, Harnessing the antitumor potential of macrophages for cancer immunotherapy. *Onco. Targets. Ther.* **2**, e26860 (2013).
54. K. B. Long, W. L. Gladney, G. M. Tooker, K. Graham, J. A. Fraietta, G. L. Beatty, IFNγ and CCL2 cooperate to redirect tumor-infiltrating monocytes to degrade fibrosis and enhance chemotherapy efficacy in pancreatic carcinoma. *Cancer Discov.* **6**, 400–413 (2016).
55. F. A. Ran, P. D. Hsu, J. Wright, V. Agarwala, D. A. Scott, F. Zhang, Genome engineering using the CRISPR-Cas9 system. *Nat. Protoc.* **8**, 2281–2308 (2013).
56. J. W. Lee, M. L. Stone, P. M. Porrett, S. K. Thomas, C. A. Komar, J. H. Li, D. Delman, K. Graham, W. L. Gladney, X. Hua, T. A. Black, A. L. Chien, K. S. Majmundar, J. C. Thompson, S. S. Yee, M. H. O'Hara, C. Aggarwal, D. Xin, A. Shaked, M. Gao, D. Liu, M. J. Borad, R. K. Ramanathan, E. L. Carpenter, A. Ji, M. C. de Beer, F. C. de Beer, N. R. Webb, G. L. Beatty, Hepatocytes direct the formation of a pro-metastatic niche in the liver. *Nature* **567**, 249–252 (2019).
57. J. H. Levine, E. F. Simonds, S. C. Bendall, K. L. Davis, E. A. D. Amir, M. D. Tadmor, O. Litvin, H. G. Fienberg, A. Jager, E. R. Zunder, R. Finck, A. L. Gedman, I. Radtke, J. R. Downing, D. Pe'er, G. P. Nolan, Data-driven phenotypic dissection of AML reveals progenitor-like cells that correlate with prognosis. *Cell* **162**, 184–197 (2015).
58. S. Van Gassen, B. Callebaut, M. J. Van Helden, B. N. Lambrecht, P. Demeester, T. Dhaene, Y. Saeys, FlowSOM: Using self-organizing maps for visualization and interpretation of cytometry data. *Cytometry A* **87**, 636–645 (2015).
59. A. H. Ko, A. C. Jordan, E. Tooker, S. F. Lacey, R. B. Chang, Y. Li, A. P. Venook, M. Tempero, L. Damon, L. Fong, M. H. O'Hara, B. L. Levine, J. J. Melenhorst, G. Plesa, C. H. June, G. L. Beatty, Dual targeting of mesothelin and cd19 with chimeric antigen receptor-

modified t cells in patients with metastatic pancreatic cancer. *Mol. Ther.* **28**, 2367–2378 (2020).
60. M. I. Love, W. Huber, S. Anders, Moderated estimation of fold change and dispersion for RNA-seq data with DESeq2. *Genome Biol.* **15**, 550 (2014).
61. Y. Hao, S. Hao, E. Andersen-Nissen, W. M. Mauck III, S. Zheng, A. Butler, M. J. Lee, A. J. Wilk, C. Darby, M. Zager, P. Hoffman, M. Stoeckius, E. Papalexi, E. P. Mimitou, J. Jain, A. Srivastava, T. Stuart, L. M. Fleming, B. Yeung, A. J. Rogers, J. M. McElrath, C. A. Blish, R. Gottardo, P. Smibert, R. Satija, Integrated analysis of multimodal single-cell data. *Cell* **184**, 3573–3587.e29 (2021).
62. V. R Core Team, *R: A Language and Environment for Statistical Computing. R Foundation for Statistical Computing* (Austria, 2021); https://www.R-project.org/.
63. I. Korsunsky, N. Millard, J. Fan, K. Slowikowski, F. Zhang, K. Wei, Y. Baglaenko, M. Brenner, P.-R. Loh, S. Raychaudhuri, Fast, sensitive and accurate integration of single-cell data with Harmony. *Nat. Methods* **16**, 1289–1296 (2019).

Acknowledgments: We thank A. Chan for assistance with cytokine assays and J. Drees for discussions. We thank all members of the Beatty laboratory for helpful discussions. **Funding:** This research was supported by the NIH grants T32-HL007439-41 (M.M.W.), K12-CA076931-21 (M.M.W.), R01-CA197916 (G.L.B.), R01-CA245323 (G.L.B.), U01-CA224193 (G.L.B.), a research grant from the Lustgarten Foundation Inc. (G.L.B.), and the Inez-Wade Fund (M.M.W.). M.M.W. is a Damon Runyon Physician-Scientist supported (in part) by the Damon Runyon Cancer Research Foundation (PST-34-21). M.L.S. is a Cancer Research Institute/Samuel and Ruth Engelberg Fellow. Additional funding support was provided by HiberCell Inc. Imprime PGG (Odetiglucan) is owned by HiberCell Inc., which manages its distribution. **Author contributions:** M.M.W. and G.L.B. designed, analyzed, and interpreted all experiments. M.M.W., H.Co., V.M.H., K.G., M.L.S., Y.X., R.B.C., S.C-B., S.K.T., H.Ch., Y.L., K.M., L.M., C.C., M.L., and M.G. performed experiments and analyzed data, under the supervision of M.M.W. M.M.W. prepared the figures. M.M.W. and G.L.B. wrote the manuscript. All authors critically revised the manuscript. G.L.B. supervised the study. **Competing interests:** M.M.W. reports prior or active roles as a consultant for Nanology. G.L.B. reports prior or active roles as a consultant/advisory board member for Adicet Bio, Aduro Biotech, Alligator Biosciences, AstraZeneca, BiolineRx, BioMarin Pharmaceuticals, Boehinger Ingelheim, Bristol-Myers Squibb, Cantargia, Cour Pharmaceuticals, Genmab, HotSpot Therapeutics, Incyte, Janssen, Legend Biotech, Merck, Molecular Partners, Monopteros, Nano Ghosts, Opsona, Pancreatic Cancer Action Network, Seagen, Shattuck Laboratories, and Verastem and reports receiving commercial research grants from Alligator Biosciences, Gilead Sciences, Incyte, Bristol-Myers Squibb, Verastem, Halozyme, Biothera, Hibercell, Newlink, Novartis, Arcus, and Janssen. G.L.B. is an inventor of intellectual property (U.S. patent numbers 10,640,569 and 10,577,417) and recipient of royalties related to CAR T cells that is licensed by the University of Pennsylvania to Novartis and Tmunity Therapeutics. N.B. is an employee of and owns stock in HiberCell Inc. V.M.H. is a current employee of GlaxoSmithKline. M.M.W., G.L.B., and N.B. are inventors on patent application number 63/505,892 held by HiberCell Inc. that covers methods of treating cancer using soluble beta glucans and CD40 agonistic monoclonal antibodies. **Data and materials availability:** Raw and processed bulk RNA-seq and scRNA-seq files are available from Gene Expression Omnibus (GEO) under accession number GSE233175. No custom algorithms were used for data analyses, and all R packages used are identified in Materials and Methods. All other data needed to support the conclusions of the paper are present in the paper or the Supplementary Materials.

Submitted 30 June 2023
Accepted 15 September 2023
Published 17 November 2023
10.1126/sciimmunol.adj5097

Science Immunology

Cancer immunotherapy via synergistic coactivation of myeloid receptors CD40 and Dectin-1

Max M. Wattenberg, Heather Coho, Veronica M. Herrera, Kathleen Graham, Meredith L. Stone, Yuqing Xue, Renee B. Chang, Christopher Cassella, Mingen Liu, Shaanti Choi-Bose, Stacy K. Thomas, Hana Choi, Yan Li, Kelly Markowitz, Lauren Melendez, Michael Gianonne, Nandita Bose, and Gregory L. Beatty

Sci. Immunol. **8** (89), eadj5097. DOI: 10.1126/sciimmunol.adj5097